PARTICLE TRACKING FOR UNDERSTANDING THE PROPERTIES AND DYNAMICS OF BACTERIAL BIOFILMS

by

Alona Birjiniuk

S.B. Chemical-Biological Engineering, Massachusetts Institute of Technology (2009)
S.B. Physics, Massachusetts Institute of Technology (2009)

Submitted to the Department of Chemical Engineering
in partial fulfillment of the requirements for the degree of

Doctor of Philosophy in Chemical Engineering

at the

MASSACHUSETTS INSTITUTE OF TECHNOLOGY

June 2015

Author..... Signature redacted
Department of Chemical Engineering
May 27, 2015

Certified by..... Signature redacted
Patrick S. Doyle
Professor of Chemical Engineering
Thesis Supervisor

Certified by..... Signature redacted
Katharina Ribbeck
Assistant Professor of Biological Engineering
Thesis Supervisor

Accepted by..... Signature redacted
Richard D. Braatz
Professor of Chemical Engineering
Chairman, Department Committee on Graduate Students

Abstract

PARTICLE TRACKING FOR UNDERSTANDING THE PROPERTIES AND DYNAMICS OF BACTERIAL BIOFILMS

by
Alona Birjiniuk

Submitted to the Department of Chemical Engineering
on May 27, 2015 in partial fulfillment of
the requirements for the degree of
Doctor of Philosophy in Chemical Engineering

Bacterial biofilms consist of surface adherent bacteria that surround themselves with a polymer matrix which provides environmental protection and antibiotic resistance. Biofilms can grow on most implanted medical devices, on heart valves, and in the lungs of patients with cystic fibrosis, resulting in difficult to treat infections that can become blood-borne and spread throughout the body. They also pose problems in industry by growing in pipes, on membrane reactors and on ship hulls. Understanding the physical properties and dynamics of biofilms is therefore of interest as such insight may lead to methods for their disruption and removal.

Biofilms have been characterized biochemically, as the general composition of the matrix is known, as are the specific polysaccharides forming the bulk of the matrix for some species. Insight into physical properties of biofilms, such as elasticity and deformability, has been limited to macroscale techniques that assess averaged values. These techniques do not provide details on the spatial gradients of physical properties within a biofilm nor do they allow for evaluation of properties over time. In addition, while some methods have been used to understand the adhesive forces of bacteria leading to biofilm formation, little effort has been put forth to understand how bacteria that are natively non-motile can reach a surface to which they adhere. Particle tracking is a technique in which probe particles are placed in a material and observed using microscopy. The observed trajectories can be analyzed in various ways, for example to determine physical properties and structure of the material they are embedded in. Trajectories can also be analyzed to better understand motion patterns of motile probes or to assess for diffusive behavior. In this work, particle tracking was used in different contexts to assess various biofilm systems. The overall goal was to gain an understanding of the structure, physical properties and dynamics of biofilms.

We first developed a method by which we performed single particle tracking in biofilms with beads of varying surface functionalization. With a combination of single particle tracking and microrheological concepts, it was found that *Escherichia coli* biofilms display height dependent charge density that evolves over time. Statistical analyses of bead trajectories and confocal microscopy showed inter-connecting micron scale channels that penetrate throughout the biofilm, which may be important for nutrient transfer through the system. This methodology provides significant insight into a particular biofilm system and can be applied to many others to provide comparisons of

biofilm structure. The elucidation of structure provides evidence for the permeability of biofilms to microscale objects, and the ability of a biofilm to mature and change properties over time.

Second, we applied particle tracking to elucidate the motions of non-motile bacteria in the presence of a motile species. In static co-culture, *Pseudomonas aeruginosa* and *Staphylococcus aureus* formed multispecies biofilms at an air-liquid interface, while monocultures of *S. aureus* were not capable of forming a biofilm at the interfacial region. Based on these observations, we tested if *P. aeruginosa* could facilitate the transport of *S. aureus* to the air-liquid interface by a motility-based mechanism. Using a cell tracking method, we compared the motion behavior of *S. aureus* in the presence or absence of *P. aeruginosa*. Our data revealed a shift in *S. aureus* motility, which changed from random motion in monoculture to directed horizontal and vertical migration when cultured with *P. aeruginosa*. Additionally, we observed a similar behavior between *P. aeruginosa/S. epidermidis* and *E. coli/S. aureus* co-cultures. Our results suggest that non-motile bacteria perhaps leverage motility from other species to promote exploration of new ecological niches. We envision that this observed behavior perhaps has significant implications during the establishment and dissemination of polymicrobial infections in the host organism.

By using multiple techniques to assess trajectories of either bead or bacteria probes, we were able to improve understanding of biofilm dynamics. The first technique can be applied to other biofilm systems, such as those formed by genetically modified bacteria, to promote a comparison of biofilm structure and properties. The second can allow for further assessment of interspecies interactions, perhaps to probe the specific mechanisms by which bacteria can attach to one another to improve motility.

Thesis Supervisor: Patrick S. Doyle
Title: Professor of Chemical Engineering

Thesis Supervisor: Katharina Ribbeck
Title: Assistant Professor of Biological Engineering

ACKNOWLEDGEMENTS

This PhD represents part of my path towards a dual MD/PhD degree, and eventually a career as a clinician-scientist. A number of people have helped me both on this specific leg of the journey as well as towards my degrees in general. I thank my advisors, Patrick Doyle and Katharina Ribbeck for the collaboration that allowed me to pursue my clinically-motivated research interests and for giving me the latitude to develop my own project. Prof. Doyle made sure that the physical insights developed were always well thought out and Prof. Ribbeck always pushed for biological relevance and insight. My other thesis committee members, Prof. Collin Stultz and Prof. Brad Olsen have provided excellent insight over the course of our meetings, and have helped push my experimental work. Prof. Stultz also deserves recognition as my MD/PhD advisor, and I am indebted to him for the excellent advice that he continues to provide.

I received funding from several sources over the course of my PhD, which have allowed me to pursue the work described here. My first year was funded by a Landau ChE Practice School Fellowship. Subsequently, I was awarded a Hugh Hampton Young Fellowship and then an NIH-NIAID F30 Fellowship (1F30AI110053), which have funded much of my research.

There are a number of people who were important to my intellectual growth before graduate school. First, I thank Prof. Hemant Thatte, my very first research mentor, for taking me in as a high school student and teaching me how to be a scientist. As an undergraduate, it was a privilege to work with Dr. Amit Agrawal in the lab of Prof. Sangeeta Bhatia. They taught me how to be an independent researcher, and provided

me with great advice during my time in the lab. Prof. Eric Hudson (now at PSU) sparked my interest in physics during my first semester at MIT, and his asking me to TA 8.02 the next semester likely led to my eventual pursuit of a physics undergraduate degree. Prof. George Stephanopoulos was my undergraduate advisor in chemical engineering, and I appreciate his encouragement of my academic choices, his interest in my being a well-rounded person, and his sense of humor. Prof. Bill Deen taught the very first class I took in fluid dynamics, inspiring what will be a lifelong fascination with the subject. He was also an early champion of the unique dual-degree path I have gone down, and has provided me with indispensable advice over the years.

I have had some great labmates in both the Doyle and Ribbeck labs. In particular I thank Jeremy, Ben, Harry and Lynna in the Doyle group for their conversations and ideas, scientific or otherwise. In the Ribbeck lab, I thank Nicole B., Julia, Tahoura and Wes for letting me bounce ideas off of them and for occasional comic relief.

Amy Cohen, the MD/PhD program administrator, has been amazing in her willingness to help me pursue my dual-degree program. In particular, she answered every question that came up as I was writing and submitting the fellowship that is funding a large portion of my education. In addition, I thank Dr. Loren Walensky, the MD/PhD program director, for his support of my unique dual-degree education, and for being an excellent example of what it means to be a leader.

I thank my friends at HMS, MIT and the Minuteman Field Hockey Club for their friendship and for making sure I had fun outside of lab. I was lucky enough to find an exceptional colleague and friend in Nicole Billings. Our complementary bodies of knowledge created a fruitful intellectual collaboration, and we have also managed to become good friends in the process. Kendele Snodgrass, one of my first-year classmates, has essentially become my third sibling over the past few years, and I am so grateful for her friendship.

Finally, I thank my family. My brothers, Joav and Jonathan, proofread my writing, listened to my ideas, and always provided some laughs when needed. Joav's creativity of thought is a constant inspiration. I have been so lucky to have Jonathan on campus during my PhD, and I enjoyed every conversation we had when we ran into each other in the hall. My parents have been nothing short of instrumental in my success, both in my PhD and before. During my time in graduate school, they have housed me, fed me, and provided me with amazing conversations. Throughout my academic career they have always been there to support and encourage me, and have been the best role models I could ask for. Thank you all for your love and for being such a warm and strong family.

TABLE OF CONTENTS

LIST OF FIGURES

LIST OF TABLES

CHAPTER 1

Introduction

1.1 Motivation

Bacterial biofilm consists of a community of bacterial cells adhered to a surface or within a scaffold. The bacteria are surrounded by extracellular polymeric substance (EPS), a polymer mixture which is secreted by the cells in response to environmental factors [1]. The biofilm, which can act as a self-healing polymer, provides protection for the bacteria, facilitating communication between cells and conferring resistance to antibiotics. Biofilms represent a major problem in the healthcare setting as indwelling medical devices (catheters, heart valves, etc.) are often sites for biofilm formation, leading to difficult to treat blood-borne infections [2]. Industrially, biofilms can lead to fouling of membrane reactors, such as those used for water purification and can deposit on ship hulls, increasing the drag they experience and thus fuel expenditure [1]. Understanding the physical properties and formation dynamics of biofilms is therefore of interest as such insight could lead to methods for biofilm disruption and removal, or

to production of polymer mimics which take advantage of the unique properties of biofilms.

Characterization of the physical properties of the EPS matrix has been dominated by the use of macroscale techniques which provide averaged values of physical properties of interest by externally deforming a sample[3]. These techniques include the use of rheometers[1,4-10], shear flow in microfluidics devices[11-14], and atomic force microscopy[15-18]. These experiments do not provide details on the spatial gradients of physical properties within a biofilm, nor do they allow us to probe heterogeneity of biofilm structure in a real-time, living system. We therefore aimed to use the technique of particle tracking, in which multiple microbeads are placed in a material and observed using microscopy, to analyze biofilm structure, allowing for the extraction of localized material behavior. In addition, it is of great interest to understand the dynamics of behavior, both temporally in a grown biofilm and in understanding key features of biofilm lifecycle, such as deposition on a surface. By applying particle tracking techniques to measure the motions of bacteria as well as beads, we gain further insight into the biofilm's ability to form and thrive.

1.2 Biofilm Structure and Dynamics

The majority of a biofilm is the EPS, which takes up about 90% of the dry weight and, *in vivo*, consists of water containing dissolved polysaccharides, as well as protein, nucleic acids, and lipids [19]. While the basic types of components of EPS are the same, the specific polysaccharides vary between bacterial strains. The ability to correlate matrix components to structural development is key to understanding the internal structure of biofilms as well as how to best disrupt them.

The most thoroughly studied EPS is that of *Pseudomonas aeruginosa (P. aeruginosa)*, a common respiratory pathogen, whose EPS polysaccharides mainly consist of some combination of alginate, Pel, and Psl. Alginate, a main component of the EPS from clinical strains of *P. aeruginosa*, was thought to be important to biofilm formation in this species until several laboratory species were not found to express alginate genes during biofilm development [20,21]. However, genetic mutations in the Psl operon are sufficient to produce biofilm-impaired strains as observed via

microscopy [22]. It has been shown that Pel does not affect the ability of bacteria to adhere to a surface and initiate biofilm formation, but is required to produce normal mature biofilm morphology [23]. More recently a group tested a wider range of bacterial strains and noticed similar external colony morphology between wild type and all mutants for biofilms grown on solid medium, though biofilms under flow exhibited different structures depending on the presence or absence of Psl [24].

As evidenced by the methods used for determining the characteristics of EPS mutants, structure and morphology characterization of biofilms is currently based on imaging techniques that allow for the visualization of fluid and bacteria. This leads to the ability to demarcate gross structures, such as wrinkled vs. smooth biofilms, or the formation of flat biofilms rather than mushroom or other irregular topologies [23,25]. Microscopy techniques have led to the discovery of several formations of biofilm, including clustered, mushroom shaped colonies through which there are large water channels, and densely-packed, flatter, surface-covering biofilms [26]. The ability to distinguish different colony types visually does provide some evidence for the changes incurred by changing biofilm matrix; however, the ability to rigorously determine internal structure and physical properties can provide a more detailed understanding of biofilm physiology.

While it is important to understand the structure of a fully-formed biofilm, insight into their formation is also helpful for determining ways to prevent their development on surfaces. The beginning of the biofilm lifecycle involves the adhesion of bacteria to a surface, with subsequent reorganization and then release of matrix components[27]. As will be described in section 1.3, the adhesive properties of formed biofilm have been examined in multiple ways[28-30], but equally interesting is understanding how bacteria reach a surface of interest. Many bacteria exhibit swimming motility, which is generally facilitated by one or more flagella[31] and allows them to move toward environments of favorable conditions[32,33]. However, multiple species of biofilm-formers are non-motile and cannot colonize by swimming to a site. Understanding how these types of bacteria reach their destinations before forming a biofilm might also be key to determining ways to prevent their formation on surfaces.

1.3 Mechanical Properties of Biofilms and Methods of Measurement

Mechanical properties arise from the internal structural organization of the biofilm, and thus methods to measure these properties can help improve the understanding of biofilm physiology. Biofilms consist of bacteria and hydrated macromolecules in water, creating a complex fluid that does not behave as purely viscous or purely elastic. Thus, characterization of their internal structure requires an assessment of both the physical properties of the biofilm on the microscale as well as any structural features that exist within it. The techniques to study these properties can also be adapted to understanding bacterial motion, providing additional insight into bacterial motility and biofilm dynamics.

Rheology is the study of the response of materials to applied forces. Traditionally, rheometry has been performed on bulk materials, and this will be referred to as macroscale or bulk rheology in later sections. More recently, the field of microrheology has arisen, which studies the local properties of materials on the microscale and allows for internally probing the mechanics of a fluid. The techniques used for gathering rheological data will be discussed in later sections, but we begin with a discussion of which properties of materials we are interested in and how they relate to biofilms. These properties are useful in characterizing the ability of a material to either flow or store energy in response to shear stress. For a more thorough discussion of rheology, we guide the reader to the books and reviews cited in this section, all excellent resources.

A Hookean solid is a material that is purely elastic, and can be modeled mechanically as a spring. These materials store energy as they deform under stress and can then relax back to their original shape. Hookean solids exhibit the following stress/strain relationship, where E represents the Young's modulus of the material, σ is the shear stress, and γ is the shear strain[34]:

$$E = \sigma/\gamma \qquad \text{(Equation 1-1)}$$

A Newtonian liquid acts in a purely viscous manner, meaning that it flows and dissipates energy in response to stress. Such materials can be modeled as dashpots, yielding a different stress/strain relationship [34]:

$$\sigma = \eta\dot{\gamma} \qquad \text{(Equation 1-2)}$$

In this case, η represents the viscosity, and $\dot{\gamma}$ represents shear rate. Most materials, including biofilms and other polymer systems, are neither Hookean nor Newtonian, but are instead viscoelastic. Instead of a lone spring or dashpot, these materials can be modeled most simply as a spring and dashpot in series, though more complex models exist. For these materials, we introduce a complex shear modulus that incorporates elastic storage and viscous loss [35]:

$$\sigma(\omega) = G^*(\omega)\gamma(\omega) \qquad \text{(Equation 1-3)}$$

As will be discussed later the storage modulus can be represented via two components: $G'(\omega)$, the storage modulus, and $G''(\omega)$, the loss modulus. By determining the values of these moduli, we can understand how a biofilm responds to stresses placed on it, most importantly if it acts in a more viscous or more elastic manner to a given applied stress.

In addition to viscosity, elasticity, and a complex shear modulus, we can also use creep compliance to understand the way in which a material responds to a constant applied stress. Creep compliance is defined as the ratio of strain to stress, where $J(t)$ is the creep compliance, $\gamma(t)$ is the measured strain of the material, and σ_0 is the constant stress [36]:

$$J(t) = \frac{\gamma(t)}{\sigma_0} \qquad \text{(Equation 1-4)}$$

The higher the creep compliance of a fluid, the more it deforms to a given stress, and thus by evaluating the creep compliance of a biofilm we can better understand how it will react to an applied external force. In a purely Newtonian material, the strain, and therefore compliance will increase linearly with time, whereas for a purely Hookean material there is an instantaneous increase in strain, which then remains constant over time [34,36].

Finally, it is also of interest to understand adhesion between biofilms and surfaces, as a key step to biofilm formation is the adhesion of bacteria to a surface. In general, adhesion tells us about the energy of interaction between two materials and may be determined by measuring the force required to separate two surfaces. Historically in the biofilm field, adhesive strength has been defined as follows [28,37]:

$$\xi = \frac{W}{\beta A} \qquad \text{(Equation 1-5)}$$

In the above equation, ξ is the adhesive strength in Watts/m^2, W is work required to pull a biofilm away from its substrate, A is the total surface area of a test surface, and β is the fraction of that surface covered by biofilm.

1.3.1 Bulk measurements

The most common tool in rheology is the bulk scale rheometer, which consists of either parallel plates or a cone and plate between which the material of interest is placed (Figure 1-1a). This setup allows one to apply a known stress to a material and measure the strain or vice versa, from which the complex shear modulus can be calculated. If these tools are used to apply a small strain to a fluid, we can assume that the underlying structure of the material remains unchanged and can assume a linear dependence between stress and strain [38]. Therefore, by applying a known, small, oscillatory strain (in a technique known as small angle oscillatory shear), we can measure the linear response of a fluid [39]:

$$\gamma(t) = \gamma_0 \sin(\omega t) \qquad \text{(Equation 1-6)}$$

The stress oscillates with the same frequency (ω) as the strain, but leads by a phase angle (δ) [40]:

$$\sigma(t) = \sigma_0 \sin(\omega t + \delta) \qquad \text{(Equation 1-7)}$$

These can be substituted into the following relation to determine $G'(\omega)$ and $G''(\omega)$:

$$\sigma(t) = \gamma_0 [G'(\omega) \sin(\omega t) + G''(\omega) \cos(\omega t)] \qquad \text{(Equation 1-8)}$$

This yields the following for the storage and loss moduli:

$$G' = \frac{\sigma_0}{\gamma_0} cos\delta \text{ and } G'' = \frac{\sigma_0}{\gamma_0} sin\delta \qquad \text{(Equation 1-9)}$$

Finally:

$$G^* = G' + iG'' \qquad \text{(Equation 1-10)}$$

In a creep test, a constant (rather than oscillatory) stress is applied to a material, and the resultant measurement of strain over time can be assessed. Finally, it is also possible to apply a large strain to a fluid, such that the underlying material is physically

disrupted, in order to study non-linear rheology. These measurements can provide information about shear-thinning and yield stress phenomena, via the use of step shear rate and large amplitude oscillatory shear tests respectively [41,42]. While they may not provide insight to the internal structure of biofilms, large strain measurements may be useful in understanding how to externally perturb a biofilm system. The yield stress is of particular interest, as it is a measure of how much force must be applied to an apparently solid material to get it to flow and show liquid-like behavior [43]. Multiple measurement techniques exist for finding a yield stress [43,44]. For example, the y-intercept of a curve fitted to shear stress vs. shear rate data measured in a rheometer is an approximate measure of the yield stress [43,44]. Alternatively, the yield stress can be determined directly by applying a constant stress to a material for some time, and then removing the stress. At stresses below the yield stress, the material returns to a baseline level of zero strain, whereas above the yield stress it will not fully recover from the deformation [44].

Several groups have measured the macrorheology of biofilms [1,4-10]. These prior studies can be divided into two types: those that scraped biofilms from their original growth locations to place them into a rheometer versus those that grew biofilms directly on a rheometer plate. Scraping biofilms from their original growth location may disrupt their structure, however this approach provides some additional freedom in choosing growth conditions. Several groups have used these methods to fit biofilm viscoelastic behavior to mechanical models that are more complicated than a simple spring and dashpot in series [4,5]. In addition, macrorheology has been used to assess the effect of different treatments on the properties of biofilms [1,6,7]. While the results of multiple groups indicate the biofilm is a shear-thinning fluid, the measured shear moduli range over three to four orders of magnitude, from 10^{-1} to about 10^{3} Pa. These experiments were performed using different species of bacteria and different growth methods, both of which could help explain the variation in measured moduli.

Less traditional methods for small-scale bulk rheometry have been developed to measure biofilm physical properties. One method is to grow biofilms in microfluidic devices and then apply known shear stresses by varying fluid flow [11-14]. This method allows for the measurement of stress/strain curves and adhesion of specific colonies of bacteria, though still on the bulk scale. Another method is to use a PDMS based

microfluidic device through which known stresses can be applied to microscale portions of a biofilm via changes in air pressure applied to a PDMS membrane above it [45]. While this technique does provide micrometer scale precision in the x-y plane of a biofilm, the pressure is applied to the top of the material, resulting in the measure of bulk properties.

Macrorheological studies have provided a wide range of insight into biofilm properties, including the discovery of its shear-thinning nature, shear moduli, and the effect of environment on physical properties. However, these are inherently averaged properties. Given the heterogeneous nature of biofilms, techniques that can probe spatial variations within a biofilm are of great use.

1.3.2 Passive microrheology techniques/single particle tracking (SPT)

Microrheology is used to determine the same properties as macrorheology through the use of microscale probes that are generally embedded into the material of interest [46,47]. This is of particular use for the study of biofilms and other biological materials, as it allows for the probing of the system over small length scales and can be applied without greatly disrupting a system's natural state. In addition, small sample sizes can be used, which provides great flexibility over macrorheology by allowing the use of young biofilms. The wide range of microrheological tests available allows us to test smaller-scale features of biological systems. To appropriately interpret the results of these tests, it is important to understand the way in which these techniques yield the properties of interest.

In passive microrheology, beads are embedded into a material and are not manipulated by any external force. They are therefore assumed to move in response to thermal fluctuations, of energy scale k_BT ($\sim 10^{-21}$ J at room temperature). In a typical experiment, video microscopy will be used to image the beads, and image processing software is then used to track the locations of the particle centers [48]. These locations can then be converted into individual particle traces, from which a mean-square displacement (MSD) can be extracted using the following definition:

$$MSD = \langle \Delta r^2(\tau) \rangle = \langle [r(t+\tau) - r(t)]^2 \rangle \qquad \text{(Equation 1-11)}$$

In this equation, r refers to the position of the particle in the x-y plane of an image, t is time, and τ is a lag time. The brackets indicate that this is an ensemble-average value,

though it is often practical to use an ensemble and time average. Using more exotic tracking schemes, one can also follow particle trajectories in 3 dimensions. In the discussion that follows, we will assume the MSD is from 2D traces as it is the more common observable. Experimentally, MSDs are determined from trajectories by calculating the change in position for any set of points in a trajectory separated by a given lag time and then calculating the variance of this distribution. Statistical bias may therefore appear for any experiment in which the particles are not embedded in a uniform fluid as trajectory lengths will be dependent on local microenvironment. For a purely Newtonian fluid, it is quite easy to extract a viscosity from the apparent MSD, as given by the following relationship, where r is the position of a particle, D is diffusivity, σ_{sh} is the shutter speed of the camera used, and ε is the so-called static error in particle location [49]:

$$\langle \Delta r^2(\tau, \sigma_{sh}) \rangle = 4D\left(\tau - \frac{\sigma_{sh}}{3}\right) + 4\bar{\varepsilon}^2 \qquad \text{(Equation 1-12)}$$

The static error results from the inability to completely resolve even a completely motionless probe. This error can be corrected for experimentally by measuring the motion of probes embedded in a solid, and subtracting appropriately, as seen in the last term of the equation. Though the above equation is for a Newtonian fluid, the static error correction can be applied to the apparent MSD of beads in any fluid, as it does not depend on the properties of the fluid being measured. The camera shutter speed is introduced in the above equation to account for what is known as dynamic error, which results from the motion of probes while the shutter is open and acquiring light. The longer the shutter is open and the higher the diffusivity of a probe in the fluid of interest, the larger the dynamic error will be. The correction shown above applies only to Newtonian fluids, as the mathematical form of the dynamic error changes with fluid type and is often unknown. The choice of a short enough shutter speed to minimize the effects of static error can be determined by measuring the MSD for several different shutter times and determining when shutter speed no longer significantly affects the measured MSD. For a Newtonian fluid, we can use the Stokes-Einstein relationship to relate D to the particle radius a and fluid viscosity [40]:

$$D = \frac{k_B T}{6\pi a \eta} \qquad \text{(Equation 1-13)}$$

A complex fluid does not follow the previous equation, and instead, we must use the generalized Stokes-Einstein relation (GSER), where G*(ω), represents the shear modulus in the Fourier domain, s is equal to iω, the Laplace frequency, $\tilde{G}(s)$ is the shear modulus represented in the Laplace domain, and $\langle \Delta \tilde{r}^2(s) \rangle$ is the Laplace transform of the MSD, [50,51]:

$$G^*(\omega) = \tilde{G}(s) = \frac{k_B T}{\pi a s \langle \Delta \tilde{r}^2(s) \rangle} \qquad \text{(Equation 1-14)}$$

This relationship is used to estimate the absolute value $|G^*(\omega)|$ by using a power law expansion of the MSD to calculate an approximate Laplace transform, and yields the following [51]:

$$|G^*(\omega)| \approx \frac{k_B T}{\pi a \langle \Delta r^2(\frac{1}{\omega}) \rangle \Gamma[1+\alpha(\omega)]} \text{ where } \alpha(s) = \left. \frac{d \ln \langle \Delta r^2(\tau) \rangle}{d \ln \tau} \right|_{\tau = 1/s} \qquad \text{(Equation 1-15)}$$

From this estimation of the absolute value of the complex shear modulus, we can use the following equations to determine the storage and loss moduli:

$$G^*(\omega) = G'(\omega) + iG''(\omega) \qquad \text{(Equation 1-16)}$$

$$G'(\omega) = |G^*(\omega)| \times \cos[\pi \alpha(\omega)/2] \qquad \text{(Equation 1-17)}$$

$$G''(\omega) = |G^*(\omega)| \times \sin[\pi \alpha(\omega)/2] \qquad \text{(Equation 1-18)}$$

Other, more accurate transforms, in which the power law expansion around the MSD includes higher terms have also been published [52].

Finally, the MSD also allows us to calculate the creep compliance of a material without having to deform it externally [53]:

$$J(t) = \frac{3\pi a}{2 k_B T} \langle \Delta r^2(\tau) \rangle \qquad \text{(Equation 1-19)}$$

This equation is the 2-dimensional microrheological equivalent of creep compliance. If we are indeed measuring in the linear regime, where $J(\tau)$ of the fluid is the proportionality constant between stress and strain, then all of the MSD curves of a material taken at the same temperature will collapse onto each other when multiplied by probe radius, assuming the probes are large relative to the microstructure of the material. Thus, in order to be sure that all of the above equations relating MSD to

physical properties hold true to a set of experimental values, the experiments must repeated for different probe sizes to test the validity of the assumption that the material acts like a continuum. The curves will collapse for probes that are larger than the microstructure of the probed material, so this relationship can also allow us to approximate the mesh size of a gel. The value of the creep compliance also relates to mesh density and crosslinking in a gel, and will likely decrease in value in response to an increase in either factor.

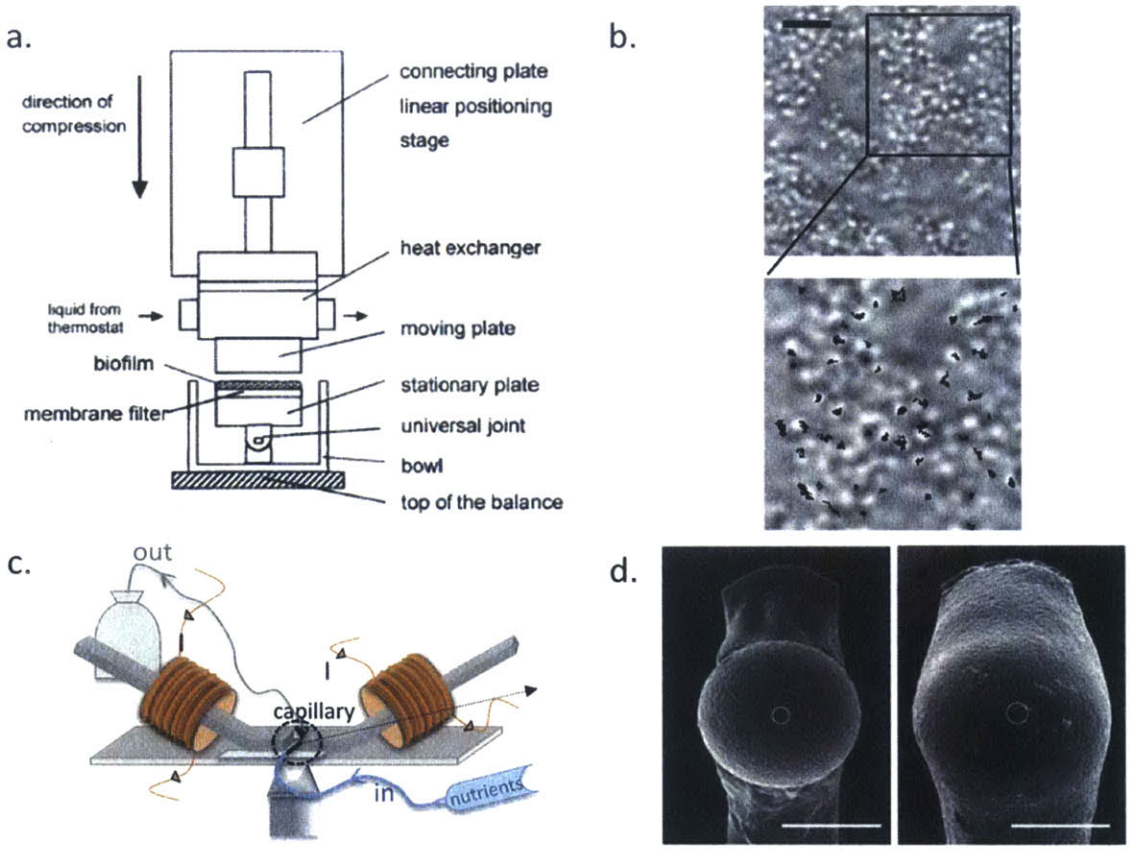

Figure 1-1. Examples of techniques that can be used to determine biofilm material properties. A rheometer setup in which a natural biofilm sample attached to a membrane can be tested (a). Reprinted with permission from [7], Copyright (2001) IWA Publishing. *Staphylococcus aureus* biofilm at 8 hours, with the tracks of bacterial motion (b). Scale bar is 5 μm. Reprinted with permission from [54], Copyright (2008) American Chemical Society. A magnetic tweezers setup for monitoring biofilms grown in flow cells (c) Reprinted with permission from [55], Copyright (2012) Elsevier. SEM images of biofilm coated beads used for AFM measurements (d). The bead on the left is surrounded by younger biofilm than the bead on the right. Scale bars are 30 μm. Reprinted with permission from [30], Copyright (2009) Elsevier.

It is important to note that the continuum assumption is not the only assumption that must be verified in order to trust the validity of an MSD to yield physical properties. Another major assumption is that the system is at equilibrium [35]. In a passive particle tracking experiment, where the particle is not being forced, this can be violated via a material that is either internally active or is aging [35]. We must be particularly conscious of both of these assumptions when applying the method to living biofilms, as they can change over time via cell turnover or secretion of new EPS, and they may be internally active if the bacteria are not completely sessile. However, if these events occur over time scales much larger than the probed time scale, which is generally the case in a biofilm where cells are dividing slowly, we can assume a quasi-equilibrium state.

Particle tracking is a versatile technique that can be modified in various ways for use in biofilms. For example, it is possible to use individual bacteria as probes for their microenvironment [54]. Using the MSDs from tracking bacteria, Rogers et al. found evidence for active motion of flagellated bacteria and were able to determine compliance of the biofilm (Figure 1-1b). This approach potentially provides a method for separating the effects of bacteria within a biofilm from externally added probes, as the two motions can be compared to one another if measured concurrently. In addition, tracking techniques can be used to determine properties of bacterial motion, both by calculating MSDs, and by applying non-traditional methods of analysis to the measured traces[56,57].

As described in the section above, macrorheological techniques have provided a wide range of values for measured physical properties of biofilms. In an attempt to reconcile these discrepancies, one group isolated the water soluble and water insoluble polysaccharide fractions from *S. mutans* biofilm and then separately reconstituted them as gels [58]. They found that the shear moduli were orders of magnitude different from each other and suggested that the water-insoluble fraction is likely part of the mechanical scaffold of the biofilm. It should be noted that this system was not applied to biofilms *in situ*, where the polysaccharide fractions are mixed with other extracellular polymeric substances that may influence the overall mechanical properties.

Recently, SPT has been used to measure the apparent diffusion coefficient of nanoparticles of varying size and surface charge within biofilms of *P. aeruginosa*, and *Burkholderia multivorans* [59]. PEGylated particles were found to have apparent diffusion constants similar to those in water, whereas positively and negatively charged particles had lower apparent diffusion constants, attributed to interaction with the biofilm. The diffusion constants similar to those in water may indicate the presence of fluid-filled channels within the biofilm system. The ability to track small particles through biofilms has also been previously used to show differences between cell clusters and voids within the biofilm, and to help measure transport rates through such a system [60,61]. Further investigation of diffusion of positively and negatively charged beads through *Burkholderia* species has been attempted to gain an understanding of potential transport of encapsulated drugs through biofilm [62].

1.3.3 Active microrheology techniques

Active microrheology is defined by the use of external force to move a probe particle through a material, rather than relying solely on fluctuations in thermal energy. Several techniques are commonly used, including atomic force microscopy, optical trapping and magnetic tweezers. These techniques allow us to overcome some of the limitations that may be encountered when attempting to use passive microrheology. In particular, much larger forces can be applied to individual particles using these techniques, which means that the linear rheology of much stiffer materials can be measured (from shear moduli of about 10^{-3}-10^{4} Pa) [63]. However, it is important to note that active forcing of particles through a soft fluid may violate the assumption of equilibrium necessary for linear microrheology, and care should be taken to appropriately calibrate the tools used for such techniques [35]. The ability to deform a material, violating the equilibrium assumption, indicates that these techniques can be used to explore the non-linear microrheology of soft fluids, as has been previously shown [64]. Another improvement over passive particle tracking is the ability to use laser detection for single particle location, which allows for more precise measurement of location and higher capture frequency (up to 10^{5} Hz), but with fewer measured particles [63].

Magnetic tweezers are used to apply a known force to a magnetic probe embedded in a material. They have been used to probe the spatial heterogeneity of

creep compliance in biofilms (Figure 1-1c), and it was found that compliance was higher further away from the surface on which the biofilm was growing [55]. In addition, the technique has been used to show that biofilm mechanical structure may be preserved under treatment with antibiotics, even if the bacteria are killed [65].

Atomic force microscopy (AFM) was developed to measure small forces and has become important in the study of polymers and living systems [47,66]. In this technique, a microscale probe is used to scan a surface and its deflections are used to determine topology or interactions between the probe and the surface. The force applied to a surface by AFM depends on the shape of the AFM tip being used, but as before, the technique measures deflection to a known force and can be used to determine rheological data. Multiple AFM and AFM-like techniques have been used to study intact biofilms, most commonly to understand their adhesive and cohesive properties. Non-AFM micromanipulators and microindenters have been used to look at the adhesive strength of biofilms grown in varying physical and chemical conditions [28,29], as well as to determine storage and loss moduli of biofilm [15]. In addition, microcantilevers have been used to apply known forces to biofilms to determine how much force is required to pull apart a biofilm, as well as to look at stress/strain curves of biofilms to calculate an elastic modulus [16-18]. AFM allows for precise force calibration, and a technique has been developed for measuring the force required to disrupt the biofilm in a location-specific manner [67]. A technique has been developed for growing biofilms onto beads attached to microcantilevers (Figure 1-1d), which allows for AFM to be performed on an intact biofilm [30]. This technique has been used to measure adhesion and stress/strain relationships of biofilms.

1.4 Overview

The goal of this thesis was to apply particle tracking techniques to better understand fundamental gaps in understanding of biofilm structure and dynamics. Following this introduction, several projects will be discussed, each of which uses the techniques described to determine unique properties of biofilms and the bacteria that form them. Finally, we will summarize this work and discuss potential future projects to further the

understanding of biofilms that is developed here. Specifically, the organization is as follows:

Chapter 1 discusses the motivation for the work, other work that has been done in the field, and provides an overview of the techniques used in the subsequent chapters.

Chapter 2 presents a project in which single particle tracking was utilized to understand spatiotemporal dynamics of biofilm structure and to elucidate structural features of the biofilm.

Chapter 3 discusses work to better understand how interspecies interactions lead to improved translocation of non-motile species and the development of unique interfacial biofilms.

Chapter 4 describes the conclusions drawn from this work and projects that spring from the results obtained.

1.5 Acknowledgement

Please note that some of the information presented in this chapter is adapted from Billings N, Birjiniuk A, Samad T, Doyle P, Ribbeck K. Material properties of biofilms – a review of methods for understanding permeability and mechanics. Rep Prog Phys, 2015 Feb 26;78(3):036601. *Review.*[68]

CHAPTER 2

Single Particle Tracking Reveals Spatial and Dynamic Organization of the E. coli *Biofilm Matrix*

2.1 Overview

In this chapter, we present a method that we developed to understand the spatiotemporal differences in biofilm properties and to elucidate biofilm dynamics. We believe that this framework can be used to understand many other biofilm systems.

The results presented here are adapted from Birjiniuk A, Billings N, Nance E, Hanes J, Ribbeck K, Doyle PS. Single particle tracking reveals spatial and dynamic organization of the *E. coli* biofilm matrix. New J Phys. 2014 Aug 27;16(8):085014. [69]

2.2 Introduction

Biofilms are formed by single-cell microorganisms that adhere to a surface, aggregate, and mature, while surrounding themselves with extracellular polymeric substance (EPS), a secreted mixture of polymers consisting mainly of polysaccharides[1]. The EPS contains nucleic acids, lipids, and proteins in addition to polysaccharides, and takes up to 90% of the dry weight of the biofilm[2]. In the healthcare setting, biofilms are associated with a multitude of disease states, such as contamination of most medical devices, endocarditis, and chronic infection of patients with cystic fibrosis[3]. These infections are particularly dangerous as biofilms are known to be resistant to antimicrobials, either by decreased antimicrobial penetration through the biofilm gel matrix, or due to lower bacterial growth rates within biofilms[1]. In industrial settings, biofilms foul membrane reactors and form on ship hulls, increasing fuel expenditure.

The desire to remove biofilms from surfaces has resulted in multiple studies to understand their physical properties, including the use of standard rheometers[4-9], microfluidics devices[10-14], atomic force microscopy (AFM)/micromanipulation[15-21], or combinations thereof [22]. These techniques have been used to assess changes in biofilm properties in response to various stressors or environmental conditions. However, these techniques all provide insight into bulk, averaged physical properties rather than yielding three-dimensional details of biofilm architecture that may influence physical properties in the native biofilm state. Further, *ex situ* approaches are often invasive and do not provide insight into dynamic changes over time. Some of the rheometry and AFM technologies require scraping of a biofilm to load a test chamber, thereby destroying its internal structure, though methods have been developed for *in situ* use of these tools[4,15,21]. The physical properties measured by these methods span several orders of magnitude due to differences in methodology, bacterial strains, and growth conditions.

Due to heterogeneity in EPS composition and structure within a biofilm, it is important to probe localized microscale properties. The use of single particle tracking thus provides an alternative to bulk measurements by examining physical properties at the microscale with high spatiotemporal resolution[23]. Single particle tracking was first used to study the properties of reconstituted EPS, derived from purifying

polysaccharides from mature biofilms[24]. Recently, a single particle tracking method was applied *in situ* to determine apparent diffusion constants of differently charged beads through biofilm, providing evidence that surface modification greatly affects mobility[25]. Bacterial tracking methods have also been employed to study the motion of flagellated and non-flagellated bacteria within biofilms, with the bacteria serving as probes for determining mechanical properties[26]. Carboxylated magnetic bead probes have been actively manipulated within *E. coli* biofilms to show spatially-dependent physical properties and the effects of environment and mutations on these properties[27]. This group showed that creep compliance increased with increasing height from the bottom of a biofilm when using carboxylated magnetic microparticles as probes, indicating a stiffer matrix near the bottom of the biofilms.

While each of these methods provides insight into biofilm structures, they do not yield a comprehensive view of an *in situ* biofilm. Thus, a single particle tracking methodology is presented here that combines several techniques and analysis methods to provide a platform for studying a native biofilm's physical properties and structures. While particle tracking is a very useful technique, it is important to recognize the complexities of interpreting data measured from a living system. Multiple groups using particle tracking to study biological materials have shown that surface properties of the probes used greatly affect the measured physical properties of the material [28-31]. In particular, surface interactions due to electrostatics or hydrophobicity alter the motions of beads of the same size, resulting in different mobilities, an indication that the beads probe both sterics and chemistry of the materials of interest. These differences must be studied in order to appropriately interpret particle tracking data acquired from such biological materials. Past work on diffusion through biofilms has shown that in other bacterial species, including *Pseudomonas aeruginosa*, *Burkholderia multivorans*, and *Alteromonas macleodii*, surface charge affects the mobility of microbeads [25,32]. Diffusion experiments on multiple species have shown that the charge of small molecules affects their ability to move through a biofilm [33]. By using multiple techniques and maintaining awareness of the complexities of the living system, the work described here probed the spatial heterogeneity of EPS, using single particle tracking to provide new information on biofilm architecture.

2.3 Materials and Methods

2.3.1 Preparation of E. coli *cultures*

E. coli EMG2[34] was used to inoculate 3 ml of lysogeny broth (LB) medium (BD) and grown on a shaker plate for 24 hours at 37°C to reach stationary phase. 100 µl of the stationary phase culture was used to inoculate 3 ml of fresh LB, and grown at 37°C with shaking to reach exponential phase. The culture was diluted in LB to 0.05 OD_{600} from an original OD_{600} between 1 and 1.5. The diluted culture was added to preformed wells constructed of PDMS bonded to a glass slide, with wells having a circular surface area, 4 mm in diameter. The cultures were grown at 37°C, without agitation, to allow for biofilm formation. Cultures grown for two days would be left undisturbed until used for experiments. For four day cultures, LB would pipetted onto the cultures at 2 days to dilute any waste products released by the bacteria and provide nutrients. Fluorescent *E. coli* EMG2 harboring a protein expression plasmid (pBBR1-MCS5-*gfp*) were cultured using a similar method, but grown in LB with 5 µg/ml of gentamicin (Sigma) to maintain the plasmid.

2.3.2 Addition of beads to biofilms

Beads were either added to the diluted bacterial culture before placement into growth chambers or after biofilm formation. Bead stock solution diluted directly into the culture solution was added in 0.05 v/v% or less. Bead stock solution added to the biofilm after growth was diluted either 1 v/v% or 10 v/v% in LB medium, and 40 microliters of solution were gently pipetted onto the biofilm culture to avoid structural disturbance. Each type of experiment was performed in triplicate. Carboxylated beads (red and yellow-green) and aminated beads (yellow-green) were purchased from Invitrogen and Polysciences. PEGylated beads were made by conjugating methoxy-PEG to the carboxylated beads as described previously[35]. Zeta potentials of beads suspended in LB were measured using a Malvern Zetasizer (Malvern).

2.3.3 Imaging of beads and analysis of motion

For bead tracking, the biofilms were imaged using an Andor iXon3-885 EMCCD camera (Andor USA) connected to an inverted fluorescence microscope (Zeiss) with a 63x oil objective (NA 1.4) to produce videos at a frame rate of 34.2 Hz with a shutter speed of 0.008 seconds. Three-minute long videos were taken at multiple points at the same height in the biofilm (as measured from the location of the glass slide), and the data

from these multiples were grouped together when analyzing a single biofilm. Locations for videos were chosen near the center of the biofilm to avoid any edge effects that might alter physical properties. Z-stack images of biofilms with beads were captured using a Zeiss LSM 510 Meta confocal microscope (Zeiss).

Particle trajectories were determined from videos using publicly available Matlab codes (Kilfoil Group, http://people.umass.edu/kilfoil/downloads.html) with slight modification. Original Matlab code was used for determining two-dimensional mean-square displacements (MSD) and all other post-processing of particle trajectories. The mean-square displacement is represented as follows:

$$MSD = \left\langle \Delta r^2(\tau) \right\rangle = \left\langle \left[r(t+\tau) - r(t) \right]^2 \right\rangle \qquad \text{(Equation 2-1)}$$

where r represents the position of a particle, t is time, and τ is a lag time. This does not account for static error in the measurement, that is the motion that would be perceived even for static beads embedded in a solid medium [36]. To correct for this, a previously described method[37] was used to measure the MSD of beads embedded in 3% agarose, assumed to be static, and this error ($\approx 10^{-5}$-10^{-4} μm^2, Appendix A.1, Table A-1) was subtracted to arrive at the final MSDs presented.

Calculated two-dimensional MSDs can be used to calculate creep compliance, the ratio of displacement to a given applied force over time[38]:

$$J(\tau) = \frac{3\pi d}{4k_B T} \left\langle \Delta r^2(\tau) \right\rangle \qquad \text{(Equation 2-2)}$$

where J represents creep compliance, d is the diameter of the probe used, T is temperature and k_B is the Boltzmann constant. Creep compliance is a material property describing deformability that should not depend on probe size assuming the probes are experiencing a homogeneous fluid, which in a gel such as biofilms means that the pore size is smaller than the probe. Given the above equation for creep compliance, scaling MSDs by bead diameter provides an indication of whether a fluid seems homogeneous at the probed length scales, and thus all graphs are presented with this scaling. As will be presented later, many of the data acquired for this system do not indicate a fluid homogenous on the probed length scales, so the value of creep compliance itself was not calculated since in this case it would not represent the actual value of the material

property. The conversion between the measured scaled MSDs and creep compliance is provided in Appendix A.2.

Table 1-1. Properties of the surface-functionalized polystyrene beads used to probe biofilms. Zeta potentials are in LB medium.

Bead Type	Size (nm)	Zeta Potential (mV)
PEGylated	1110±46	-0.3±0.5
PEGylated	2020±16	-2.6±0.5
carboxylated	516±11	-17.7±1.3
carboxylated	1100±35	-16.1±0.9
carboxylated	2000±40	-28.3±1.8
aminated	1100±35	-11.3±0.3

2.4 Results

2.4.1 Bead motion is dependent on surface charge

Biofilm EPS is formed from polysaccharides, proteins, lipids and DNA in water, and thus contains multiple types of charged moieties. It is therefore important to understand if surface functionalization of microbead probes plays a role in the mobility of beads in *E. coli* as the charged groups may interact with the charged portions of the matrix as they do in other biological systems.

To determine if bead motion is dependent upon electrostatic interactions, the motions of 1-micron aminated, carboxylated and PEGylated beads were observed. LB medium has a Debye length of less than 1 nm (see calculation in Appendix A.3), and thus differences between each bead type will depend on their interactions with local charged structures. The zeta potentials of the beads in LB medium (Table 1-1), indicate that the PEGylated beads are neutral, the carboxylated beads are negatively charged, and the aminated beads are negatively charged, with 70% of the negative charge of the carboxylated beads. PEGylated beads are considered to be generally biologically inert[39], presumably engaging in limited non-steric interactions with the biofilm. Beads one micron in diameter were added to bacteria solutions before biofilm formation ("pre-embedded") and after two days their motion was observed using the described protocol.

Bead motion was observed at three different heights in the biofilm (10, 20 and 30 microns above the glass slide, in a biofilm about 100 microns high – Figure 2-1a).

Figure 2-1b shows the scaled MSDs of the 1 micron aminated, carboxylated and PEGylated beads at 20 microns, and Figure 2-1c shows the scaled MSDs at all heights at which MSDs were measured. The PEGylated beads exhibited greater mobility than both the carboxylated and aminated beads at all locations in the biofilm. In addition, at all heights the carboxylated beads were more mobile than the aminated beads, so the mobility of the beads is not monotonic with zeta potential. The carboxylated beads contain only negative surface charge, whereas the aminated beads likely contain a mix of negative and positive surface charges as they are constructed by linking amines to carboxylated beads. Biofilms contain a mix of positively and negatively charged species, but contain more anionic species, so the mixed surface charge beads can likely form more ionic interactions leading to greater confinement [2,40,41]. Charge interactions are therefore important when examining motion of probes within *E. coli* biofilms, and must be considered in addition to spatial confinements. While it is not certain that hydrophobic interactions play a role in the differences between bead motions, the polysaccharides that form the bulk of biofilm matrix are not known to have large hydrophobic domains. In addition, while not all the proteins within the biofilm have been characterized, the *E. coli* strain used does not produce proteins known to contribute to hydrophobicity in biofilms [42-45]. Thus, the differences seen in bead motion between the different surface charges are likely due to ionic rather than hydrophobic interactions.

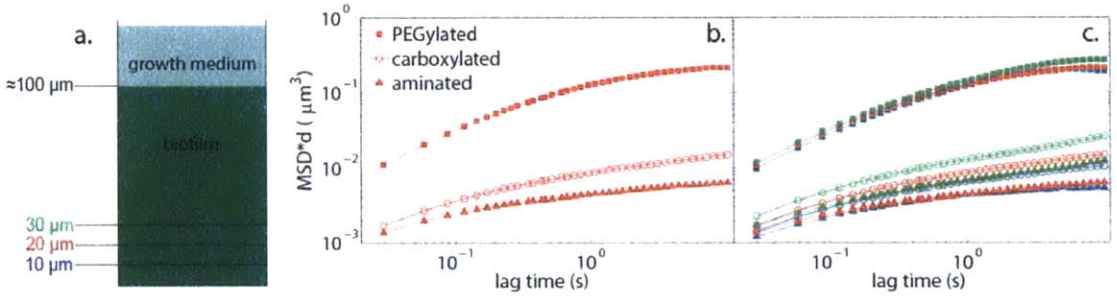

Figure 2-1. Bead motion in biofilms is dependent upon surface functionalization as shown by the motions of beads of the same size (1 μm in diameter), but different charges. (a) A schematic diagram of the biofilm showing the three heights at which MSDs were measured. Color labels (blue red and green) are defined for each height which are used to label data in panels (b) and (c). (b) MSD versus lag time for the beads at the 20 micron height. The PEGylated (neutral) beads were the most mobile, followed by carboxylated (negatively charged) and aminated (less negatively charged) beads. These data indicate that any confinement seen with charged beads is not necessarily due to mesh size alone, as if this were the case the three curves would be similar. (c) MSD versus lag time at 10, 20 and 30 microns above the bottom of the biofilm, represented by blue, red, and green lines respectively. Symbols are the same as in (b) and colors defined in (a) denote the height at which the measurement was taken.

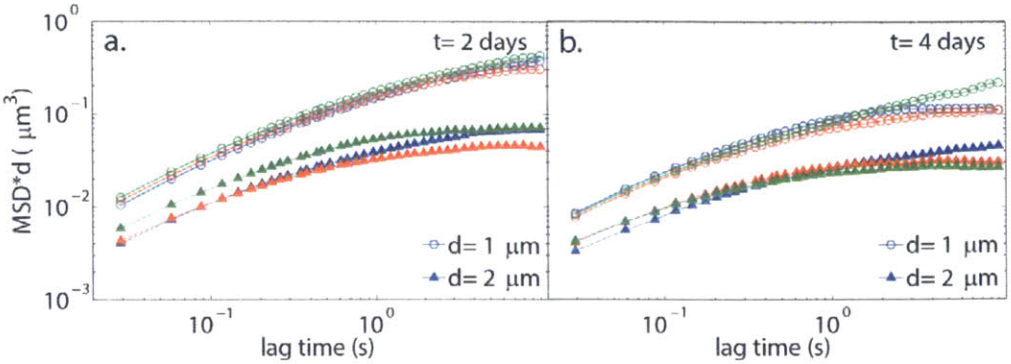

Figure 2-2. The motion of PEGylated beads in biofilms is size dependent at both 2 and 4 days. This indicates that the beads are experiencing different microenvironments, potentially due to the biological materials of the biofilm growing around the beads, as biological materials interact very little with the polyethylene glycol coating of the beads. The decrease in MSD with biofilm age with the PEGylated beads indicates that they are experiencing increased steric confinement likely due to an accumulation of biological materials, resulting in smaller regions for the beads to move in. The blue, red and green symbols represent heights of 10, 20 and 30 microns above the bottom of the biofilm respectively.

2.4.2 Biological material accumulates over time in biofilm

PEGylated beads exhibit few interactions with biological materials [39,46,47] and are charge neutral so their motion in the biofilm is likely dependent primarily on steric confinement. Studying the motion of PEGylated beads embedded within a biofilm thus provides a measure of how much solid material surrounds the beads, and if this changes over the course of biofilm development. The MSDs of 1 and 2 micron PEGylated beads embedded in biofilms were measured at two and four days of growth (Figure 2-2a and 2-2b respectively). As shown in Figure 2-2, the motion of PEGylated beads embedded in biofilms was found to be size dependent at both two and four days of growth. These results suggest that the PEGylated beads of different sizes experience unique microenvironments, perhaps the result of biological materials forming around the PEGylated beads with which they do not interact. The motion is not location dependent, which indicates that the mode of confinement is similar throughout the probed areas of the biofilm for each bead size.

Mobility of beads in a four day biofilm was reduced as compared to a two day old biofilm (Figure 2-2a,b), though again the motion is size but not location dependent. PEGylated beads are presumably experiencing steric confinement, so any decrease in mobility can be attributed to increased crowding of the probes by biological materials.

This increased confinement observed is likely due to the accumulation of material from bacterial multiplication and/or release of additional EPS components as no solid materials are externally introduced into the biofilm over its growth period.

2.4.3 Charge density in biofilms is spatially heterogeneous, with higher density near the substrate

By measuring the motions of carboxylated beads (the base bead on which the other types are constructed) in addition to PEGylated beads, it is possible to distinguish between charge-dependent and steric interactions, and to determine which ones are impacting measured materials properties. This is important as recent work has indicated that in *Staphylococcus epidermidis*, viscoelasticity is likely mediated by self-interactions between various components of the EPS, rather than entanglements of the polysaccharides due to topological constraints[48].

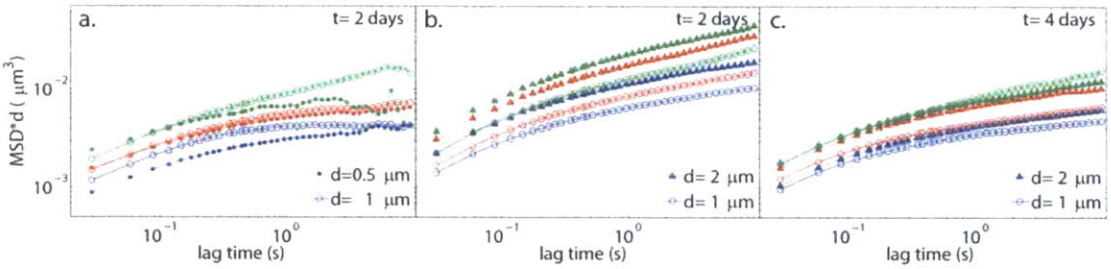

Figure 2-3. The motion of carboxylated beads within *E. coli* biofilms. (a) Carboxylated beads 0.5 and 1 micron in diameter in a two day old biofilm have MSD curves that collapse on each other at each height when scaled by bead size. (b) Beads 1 and 2 microns in diameter do not show similar scaled MSDs at each height at 2 days, and counterintuitively, the MSDs for the larger beads are bigger, indicating that they are more mobile. (c) At 4 days, the MSD curves for the 1 and 2 micron beads get closer to overlapping at each height, indicating that the beads are getting closer to both experiencing a homogenous environment. Neither set of curves resembles those produced by beads confined due to sterics alone, as seen with PEGylated beads. The beads are thus confined by charge interactions, which are height dependent, and not strong enough at 2 days to restrict a 2 micron bead to the same extent as the smaller beads. The increased confinement of the largest beads at 4 days of growth indicates that there is an increase in charge density over time, perhaps due to bacterial secretion of additional biological materials. The blue, red and green lines represent heights of 10, 20 and 30 microns above the bottom of the biofilm, respectively.

If the microbead probes in a gel mesh are experiencing a homogeneous environment, then the MSDs scaled by diameter should collapse onto each other. The scaled MSD curves for carboxylated beads 0.5 and 1 micron in diameter in a two day old biofilm overlap each other at each location, which would seem to indicate that the biofilm is homogenous on this length scale at each height (Figure 2-3a). If this result

was due to EPS pore size alone, then larger probes would have similar MSDs. However, when the scaled MSDs for 1 and 2 micron diameter beads are compared at two days, they do not collapse onto each other (Figure 2-3b). The MSDs for the 2 micron beads are larger than for the 1 micron beads, indicating that they are less confined (Figure 2-3b). At four days the pattern changes and the 1 and 2 micron bead curves are closer to overlapping (Figure 2-3c). This pattern of behavior would not be expected if the smaller beads are confined sterically. The strong dependence of mobility on charge suggests the confinement of carboxylated beads in *E. coli* biofilms is due to interactions with charged portions of the EPS matrix. The higher MSDs for the larger beads at 2 days could then be the result of the inability of the charge density at that age to arrest the motion of these beads to the same extent as the smaller beads. The height dependence of MSDs indicates that the charge density decreases at higher parts of the biofilm, either due to changes in pH of the surrounding medium from bacterial metabolism or the presence of different types or amounts of EPS components. The change between two and four days corroborates the prior conclusion that EPS materials are being released over time into the biofilm, and could also be due in part to changes in localized pH over time.

Alternatively, the charged beads may be binding to released bacterial products, which would change their surface properties over time, resulting in the different patterns of motion at different times. However, the PEGylated beads would not experience such interactions, suggesting that the addition of material to the biofilm must play some role in the altered dynamics. The biofilm is therefore actively developing over time.

2.4.4 Biofilms contain micron scale, fluid-filled channels

Biofilms are known to be heterogeneous based on chemical gradients[49,50], but their mechanical heterogeneity is not well understood. The presence of channels and voids to facilitate transport in biofilms has been suggested for several types of biofilms, based on visualizations of channels tens of microns in diameter with dye or microbeads [51,52]. Some of these channels penetrate through biofilms, whereas others are spaces between the stalks of mushroom shaped biofilm colonies. To date, there has been no direct comparison of probe motion within various regions of the EPS to provide evidence that channels with properties distinct from that of the gel penetrate the biofilm gel. To

provide such a comparison, beads were added onto an already-developed biofilm in order to compare their motions to those of beads pre-embedded in a biofilm. By using both measurements on the same system, it is possible to understand if channels are present, and if they are intrinsic to the system itself.

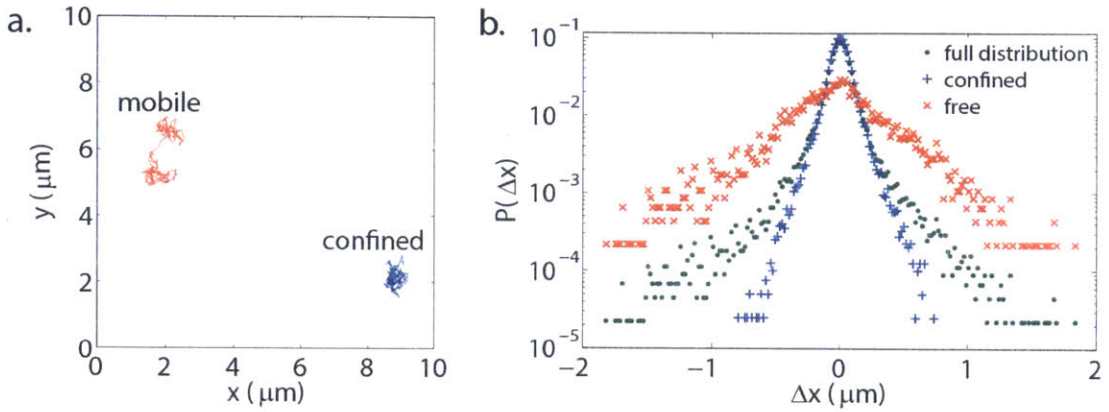

Figure 2-4. Beads added after biofilm growth exhibit two distinct types of motion. (a) Adding 0.5 micron diameter carboxylated beads onto a two day old biofilm qualitatively yielded two types of bead trajectories - some that seem mobile and others that seemed confined to a particular location within the biofilm. In this image, the mobile trajectory is 4.9 seconds long, whereas the confined trajectory is 5.6 seconds long. (b) The van Hove distribution for all the beads, shown with the distribution for the statistically separated confined and free distributions at 1 second of lag time. At small Δx, the confined distribution envelopes the full distribution, whereas at larger Δx, the free distribution envelopes the full distribution. The two distinct populations indicate beads that are experiencing two different complex fluids, likely some within channels and others associated with the EPS.

A linear fit of the MSD data for pre-embedded 0.5 micron beads (seen in figure 2-3a) at short lag times to approximate an apparent diffusion coefficient yields $D_a \approx 0.01$ μm²/s. Based on confocal images of the biofilms, they are approximately 100 μm in height, which means that a lower bound on the time it would take for beads added on to a biofilm to travel through the biofilm matrix itself and reach the bottom surface would be about 12 days. However, when the beads were added onto an already grown biofilm, a concentration front reached the bottom surface on the order of hours, indicating that the beads must be traveling through something other than the dense EPS matrix probed by the pre-embedded beads. If beads were to travel through straight, water-filled channels into the biofilms, where $D \approx 1$ μm²/s then the time for the concentration front to reach the bottom of the biofilm would be about 3 hours, which is much closer to

observed time. This indicates that the beads are likely passing through fluid-filled channels that penetrate the EPS matrix.

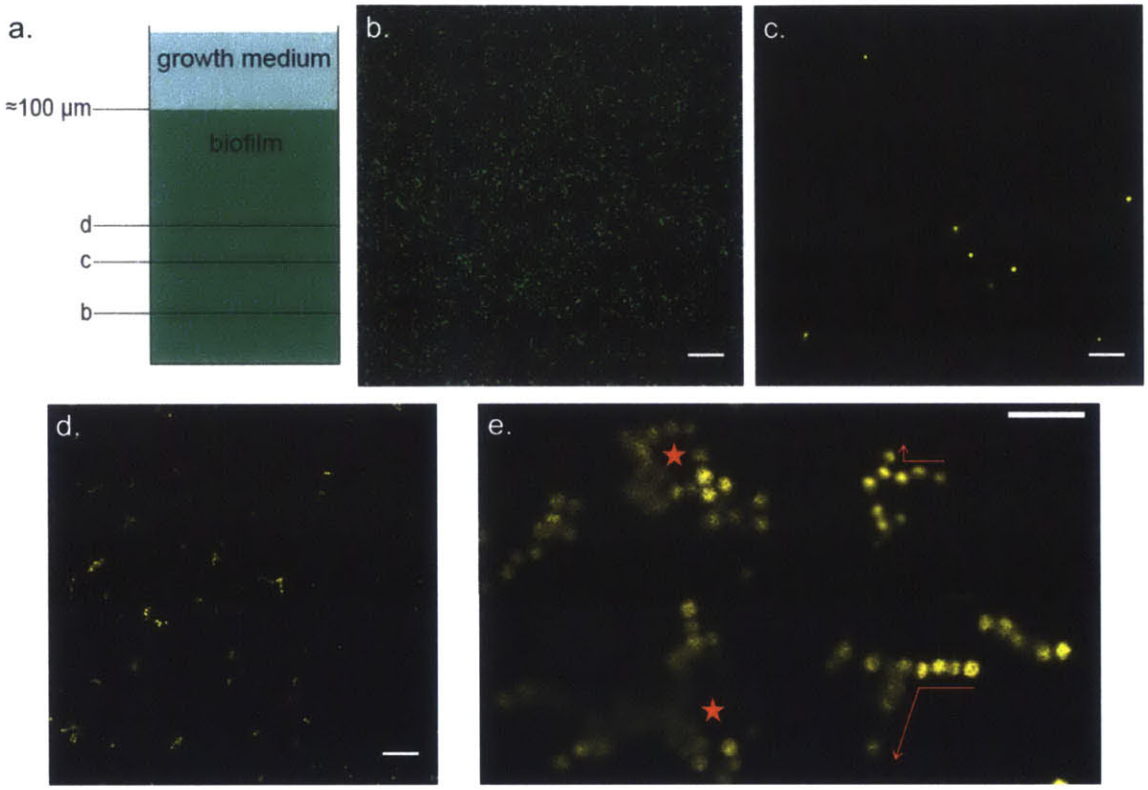

Figure 2-5. Confocal microscopy of fluorescent biofilms with 2 μm beads added after growth shows several characteristic regions after 5 hours. (a) Schematic diagram of image locations. (b) From 0-30 microns from the glass surface, only bacteria are seen in the biofilm. (c) From 30 to about 50 microns above the coverslip, many bacteria and a few lone beads are seen. (d) Above the bacteria are branched bead aggregates, with few to no surrounding bacteria. These aggregates continue higher but were not visible past 80 microns due to objective working distance. (e) Close up view of selected aggregates, which show long, branched chains (red arrows) and some keyhole shapes (red stars in center). In all panels, the bacteria are colored green and beads are colored yellow. Scale bars are all 20 μm.

Qualitatively, videos of the 0.5 micron carboxylated beads added onto a grown biofilm seemed to contain two populations of beads, some mobile, and some that seemed confined within the matrix (Figure 2-4a). To determine if these were actually two separate groups, the self-portion of the van Hove correlation was calculated. This correlation measures the probability that a particle is at a position x at a given lag time ($x(\tau)=x$), assuming that a particle was at position 0 at time 0 ($x(0)=0$), which is shown graphically by plotting the probability distribution of the step sizes made by the tracked particles for a given lag time (Figure 2-4b). If the particles are undergoing Brownian

motion in a homogeneous fluid, then the van Hove distribution should be a Gaussian. However, for the raw data, this distribution is clearly not a Gaussian, given its sharp central peak (Figure 2-4b). A previously described unbiased statistical method [53] was used to separate the beads into two populations (mobile vs. confined). In short, the range and standard deviation of each individual particle trajectory were multiplied together to produce a measure of particle mobility, and an approximate cutoff for this value was determined to separate the two groups, with the beads associated with values above the cutoff identified as mobile. In this case, the cutoff chosen is 0.2 μm^2. The two populations of beads formed distinct distributions, which envelope the inner and outer regions of the combined distribution (Figure 2-4b). This is an indication that the beads are in two different materials, likely fluid-filled channels and the EPS matrix. The confined beads likely correlate to beads associated with the EPS matrix, indicating that the interaction with the matrix is dynamic over the course of experimental time.

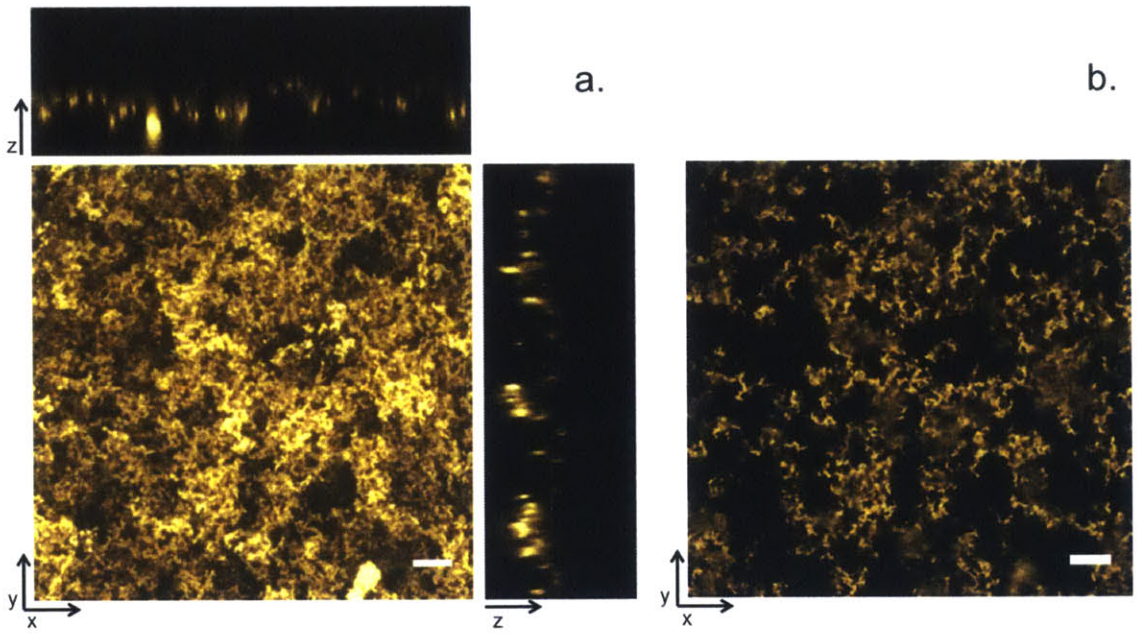

Figure 2-6. Images of a biofilm 24 hours after the addition of a high concentration of 0.5 micron diameter beads to the culture. (a) Projection of a z-stack in the z direction. If one were to lie on the slide on which the biofilm was grown and look up, this is what would be seen. The brighter regions indicate what is closer to the bottom, so it is clear that there are a few branches that reach the bottom of the biofilm, and that further up there is a high density of intersecting channels. The top and side bars show the side-view in the x and y planes, respectively. These also show some regions of deeply penetrating channels and a non-uniform top surface. Each of the side views is 73.5 μm in height. (b) An individual z-slice, about 50 microns from the bottom of the biofilm. This shows a single plane of intersecting channels. All scale bars are 20 μm.

Carboxylated and PEGylated beads 0.5 and 1 micron in diameter both diffuse through biofilms on the order of hours. However, when larger, 2 micron diameter beads were added to biofilms, few to no beads were seen at the bottom. Z-stacks acquired using confocal microscopy showed that for the first 40-50 microns of biofilm height over the growth surface there were few to no beads and densely packed bacteria (Figure 2-5a-c). Above 40 microns, long, branched clumps of 2-micron beads were observed. These bead formations were relatively static and formed multiple types of shapes including keyhole-like structures (Figure 2-5a,d-e). The lack of bacteria in this region indicates that the beads are surrounded by EPS, and the long, branched structures are indicative of beads getting stuck in channels that are too small for them to get through, providing visual evidence for the channels that could transport smaller beads through the biofilms. To more clearly image the proposed channels, highly concentrated solutions of 0.5 micron diameter carboxylated beads were added onto already grown biofilms, and allowed to diffuse through for 24 hours. After 24 hours, the biofilms were imaged, which revealed beads in highly branched channel-like formations (Figure 2-6). There were fewer channels near the bottom surface of the biofilm, and a dense network at higher spatial locations, as seen in the projection of the 3D stack (Figure 2-6a). A sample of a particular location, 50 microns above the bottom of a biofilm, shows channel-like structures that connect to the planes above and below (Figure 2-6b).

2.5 Conclusions

By combining single particle tracking, statistics, and confocal microscopy to analyze a single biofilm system, multiple structural features were elucidated. *E. coli* form biofilms with height-dependent charge density that changes with time. The physical density of the biofilm also increases with time, indicating a metabolically active system. Finally, channels exist that run through the biofilms, allowing for the passage of small molecules and micron-scale objects while limiting passage of larger objects. The wide range of features probed with this methodology makes it a useful tool for analyzing other biofilm systems, in particular for comparison of native and mutant species to determine how genetic changes influence structure formation.

CHAPTER 3

Flagellated Bacteria Transfer Staphylococcal Stowaways to New Ecological Niches

3.1 Overview

This chapter contains work done to understand the interspecies interactions that lead to unique interfacial biofilm formation. It also presents additional ways in which trajectories can be analyzed to determine the properties of a system. This work was done in conjunction with Nicole Billings, who performed the experiments that resulted in Figures 3-1, 3-2 and 3-5.

The results presented in here are adapted from Billings N*, Birjiniuk A*, Crouzier T, Doyle P, Ribbeck K. Flagellated bacteria transfer Staphylococcal stowaways to new ecological niches. 2015.

3.2 Introduction

Bacteria often exist as diverse mixed species communities in a multitude of environments [70-72]. Multispecies microbial communities are associated with eukaryotic hosts, including the human body, and often adopt a symbiotic relationship for optimal health of both the host and inhabiting microbes [73,74]. However, opportunistic pathogens that contribute to the microbiome can also establish infections within an immunocompromised or injured host. While many opportunistic microbes have been well studied regarding their impact on human health, the interactions of these organisms with other pathogens or commensal species in relation to disease outcome is of high biomedical significance. Such interactions have not been thoroughly studied, and here we attempt to elucidate the ways in which bacteria in the same community may affect each other's motility.

To find ideal environmental niches or to spread between hosts, bacteria must use various dispersal mechanisms. Most simply, bacteria are spread via contact with infected surfaces, as is seen by skin infections from bacteria entering cuts, or the spread of hospital-based infections from inadequate handwashing [75,76]. Certain bacteria are also spread via direct contact with infected fluids, and can be spread between hosts in this manner [77,78]. Dispersal can also be more efficient than via direct contact, as many bacteria can spread by droplets. In this case, bacteria are in the aerosolized fluid, and can land on whichever surface appears as they are suspended [79,80]. However, these mechanisms do not explain how bacteria might travel within a host once they have arrived.

Swimming motility offers a considerable advantage for bacteria by enabling movement toward environments of favorable conditions [32,33], movement away from toxins or predators [81,82], and the ability to efficiently colonize a host [83]. Furthermore, motility is a significant virulence factor that is intimately associated with effective host invasion and colonization [84]. *P. aeruginosa*, *E.coli*, and *H. pylori* are a few examples of pathogens that utilize flagella-driven motility during host colonization [85-87]. Non-flagellated bacteria do not have the capacity to independently translocate with this mechanism. The genus *Staphylococcus*, for example, is classically considered non-motile in fluid environments due to the lack of flagella [88,89]. Despite their limitations

in motility, Staphylococcal species are robust colonizers of the mammalian skin, wet epithelia, and the mucus barrier [90-93]. At present, mechanisms describing how non-motile bacteria reach their final destinations within a host remain elusive.

3.3 Results

3.3.1 In the presence of PAO1, S. aureus *can localize to air-liquid interface biofilms*

We tested if non-flagellated species may benefit from the swimming motility of flagellated bacteria. To address this, we studied two opportunistic human pathogens that are found in the same ecological habitats within the human host, but rely on different mechanisms for translocation. *Staphylococcus aureus* is a gram-positive, non-motile cocci species and *Pseudomonas aeruginosa* is a gram-negative, flagellated rod species capable of swimming motility. First, we cultured *P. aeruginosa* PAO1 and *S. aureus* UAMS-1 in separate micro-wells with glass or polydimethylsiloxane (PDMS) vertical inserts (Appendix B, Figure B-1) without agitation. Due to lack of swimming motility, we expected *S. aureus* to settle and form a biofilm at the bottom of the micro-well while the motile *P. aeruginosa* should build a biofilm at the air-liquid interface, which requires upward swimming motility. At 0 and 24 hours, we examined the spatial distribution of biofilm formation on each of the vertical inserts, and noticed a clear and expected difference between the strains when cultured independently (Figure 3-1a,b,d,e; Appendix B, Figure B-1b; Appendix B, Figure B-2a,b). *S. aureus* cultured alone did not readily colonize the air-liquid interface (Figure 3-1b,e; Appendix B, Figure B-1b, d; Appendix B, Figure B-2b) and at 24 hours most of the adherent biomass was localized to the bottom of the micro-well (Appendix B, Figure B-1b). By 24 hours, *P. aeruginosa* formed a biofilm along the vertical distribution of the micro-well insert, with the greatest concentration of biomass at the air-liquid interface ~5mm above the bottom of the micro-well (Figure 3-1a,d; Appendix B, Figure B-1b, c; Appendix B, Figure B-2a). However, when the two species were co-cultured in the same microwell, spatial characteristics of *S. aureus* biofilm formation were altered. In the presence of *P. aeruginosa*, *S. aureus* was more frequently observed at the air-liquid interface biofilm at 24 hours (Figure 3-1c,f; Appendix B, Figure B-2c).

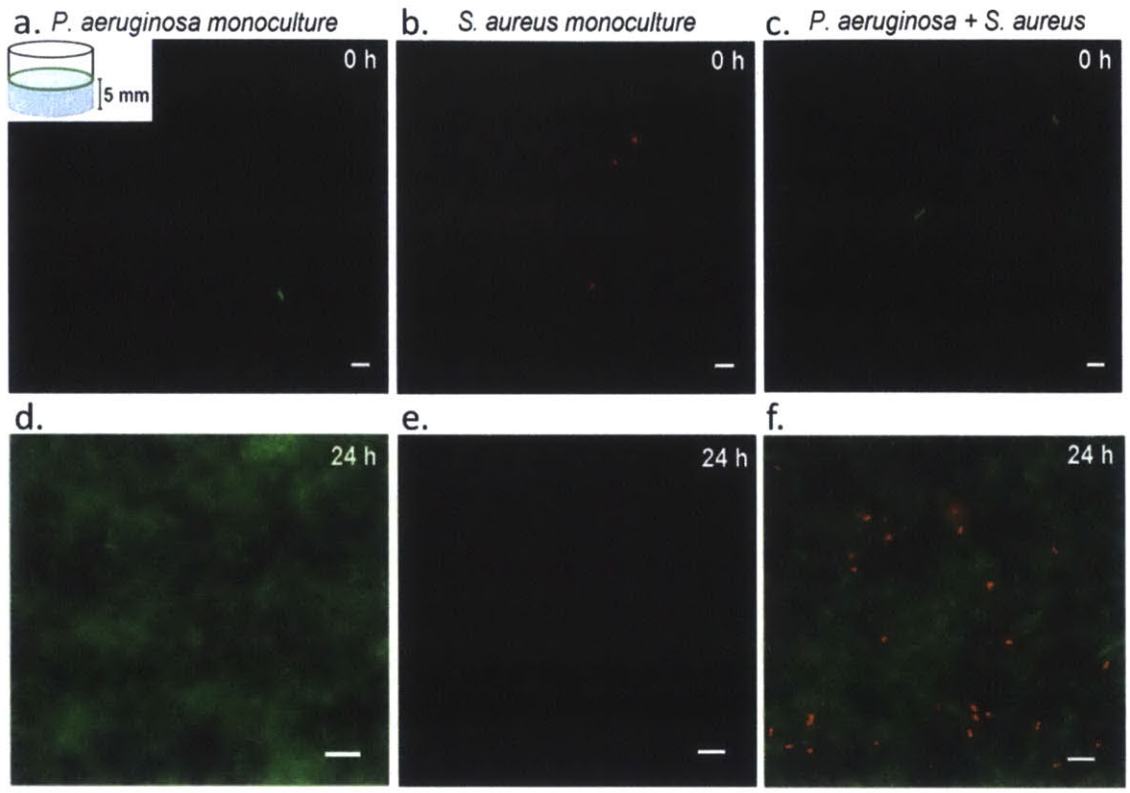

Figure 3-1. *P. aeruginosa* augments *S. aureus* localization to air-liquid interface biofilms. Microscopic observations of *P. aeruginosa* (a,d) and *S. aureus* (b,e) at the air-liquid interface of glass vertical inserts at 0 and 24 hours. *P. aeruginosa* (green) readily formed a biofilm at the air-liquid interface after 24 hours while *S. aureus* (red) sparsely populated the interfacial region. Co-culture of the two species increased localization of *S. aureus* to the air-liquid interface after 24 hours. (c,e) Scale bars represent 5 μm.

For *P. aeruginosa* alone, few cells were detected at 0 hours and there were 4 orders of magnitude more at 24 hours, reflecting the time it takes to build the biofilm at the air-liquid interface (Figure 3-1a,d; Figure 3-2a). *S. aureus* alone showed similarly low numbers at 0 and 24 hours, indicating that the bacterium by itself does not efficiently colonize this specific area (Figure 3-1b,e; Figure 3-2b). In contrast, in the presence of *P. aeruginosa*, *S. aureus* CFUs increased over 3 orders of magnitude over 24 hours when compared to the *S. aureus* monoculture (Figure 3-1c,f; Figure 3-2b). Scanning electron micrographs confirmed co-localization of *P. aeruginosa* and *S. aureus* at the interfacial region (Figure 3-2c,d). Furthermore, calculation of the terminal velocity of *S. aureus* reveals a sedimentation rate of about 55 μm/hour in the downward direction. Hence, we conclude that it is unlikely that the increased accumulation of *S.*

aureus is due to trapping within a preformed *P. aeruginosa* biofilm, as the bacteria would sediment away from the interfacial portion of the insert, well before the biofilm was formed (Appendix B.1, B.2). Instead, these data indicate that *S. aureus* has acquired, through *P. aeruginosa*, an increased capacity for traveling larger distances.

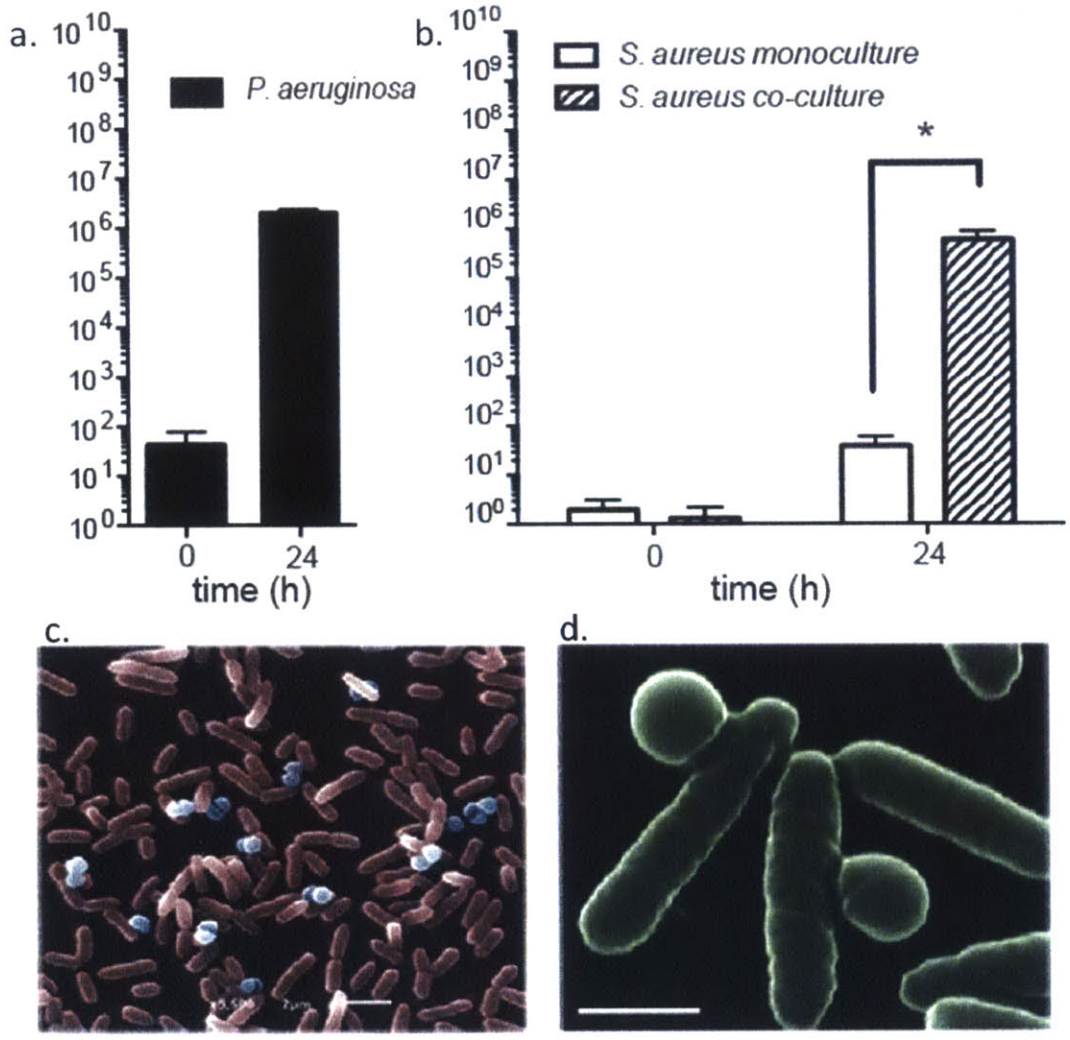

Figure 3-2. *S. aureus* is not trapped in a pre-existing *P. aeruginosa* biofilm, but rather accumulates in the interfacial biofilm over time. (a,b) Colonization of the air-liquid interface was quantified by determining the CFUs for both monocultures and co-culture. CFUs at the start of each experiment showed only a few cells at the air-liquid interface for all conditions. This indicates that a *P. aeruginosa* biofilm matrix did not initially trap *S. aureus* cells at the onset of the experiment since a *P. aeruginosa* biofilm required time to accumulate. (c,d) False colored scanning electron micrographs of *P. aeruginosa* (rod cells) and *S. aureus* (spherical cells) localization at the air-liquid interface after 2 hours revealed onset of co-localization upon the initial attachment stage of biofilm development. Scale bars in (c, d) represent 2 μm and 1 μm respectively.

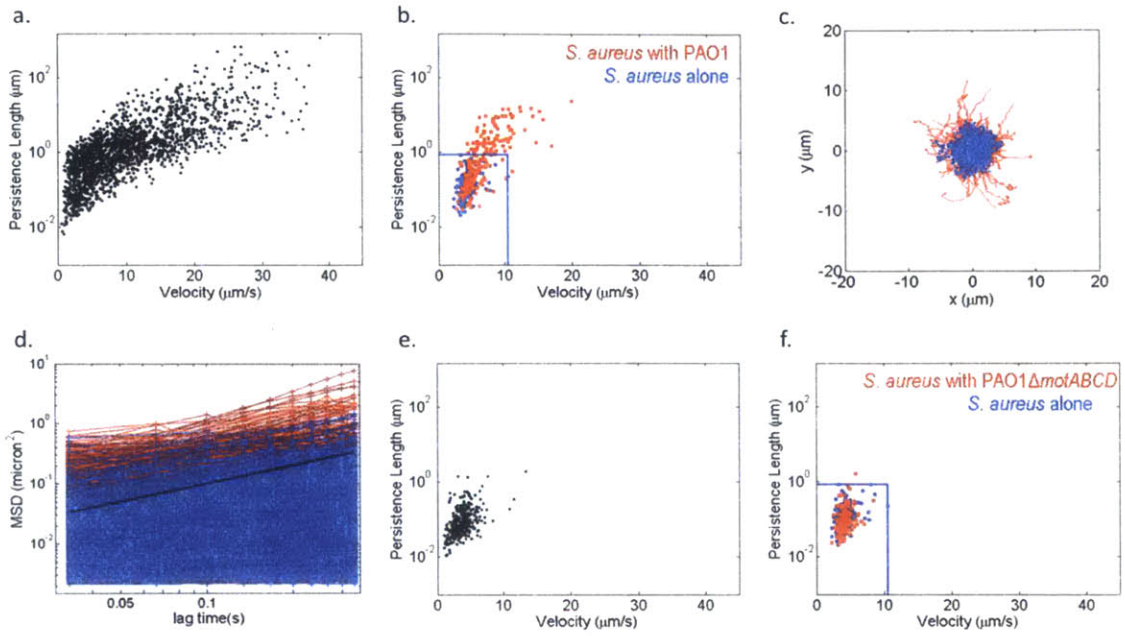

Figure 3-3. The motility patterns of *S. aureus*, *P. aeruginosa*, and *P. aeruginosa* PAO1Δ*motABCD* alone and in combination. (a) Individual trajectories of *P. aeruginosa* alone in culture plotted on axes of persistence length vs. velocity. (b) The trajectories of *S. aureus* alone (blue), and of *S. aureus* in the presence of *P. aeruginosa* (red) plotted on axes of persistence length vs. velocity. The solid lines indicate the upper bound of persistence length and velocity for the *S. aureus* alone. There is a cluster of trajectories in the mixed culture with persistence lengths several orders of magnitude higher than those in the central cluster for the *S. aureus* alone. (c) The actual traces represented in (b) re-centered to begin at coordinate (0,0) using the same color code. There is a set of trajectories in the mixed culture that are further reaching and more linear than those of *S. aureus* alone. (d) The MSD of all individual trajectories, using the same color code. There is an increase in motility of the S. aureus in the mixed culture, as seen by the higher MSDs. (e) Individual trajectories of PAO1Δ*motABCD* alone in culture, exhibiting smaller persistence lengths and velocities than *P. aeruginosa*. (f) The trajectories of *S. aureus* alone (blue), and of *S. aureus* in the presence of PAO1Δ*motABCD* (red). The motility pattern of the *S. aureus* is preserved in the mixed culture.

3.3.2 Motion of non-motile bacteria is altered in culture with motile species

The change in spatial distribution of *S. aureus* in the presence of *P. aeruginosa* could be influenced by physical interactions between the two species that promote a co-swimming behavior. To test for this possibility, we employed single cell tracking to quantify changes in the motility behavior of *S. aureus* in real time. For tracking experiments, we used wild-type strain *P. aeruginosa* PAO1 expressing enhanced green fluorescent protein (eGFP) and wild-type strain *S. aureus* UAMS-1 stained with hexidium iodide. First, we tracked the motility patterns of PAO1 and UAMS-1 individually using video microscopy, and calculated the velocity and persistence length

of each trajectory (Figure 3-3a,b). Persistence length is defined as the length scale of decay for angular autocorrelation of a trajectory, which provides a measurement of how linear a trajectory is, for each cell trace. *S. aureus* showed random motion patterns (Appendix B, Figure B-3a) with maximum persistence lengths on the order of 1 μm or less (Figure 3-3b), and mean square displacement (MSD) similar to a sphere undergoing Brownian motion in liquid medium (Appendix B, Figure B-4). For comparison, *P. aeruginosa* exhibited a run-reverse motility pattern consistent with previous accounts of swimming motility among this species (Appendix B, Figure B-3b). *P. aeruginosa* also exhibited greater velocities and persistence lengths than non-motile *S. aureus* (Figure 3-3a; Appendix B, Figure B-5a, b). However, when *S. aureus* was mixed with *P. aeruginosa*, we observed a distinct change in *S. aureus* trajectories (Figure 3-3b, c; Appendix B, Figure B-3c-e), with the persistence lengths increasing by an order of magnitude when compared to values obtained for *S. aureus* monoculture (Figure 3-3b, c). Trajectories set to start at coordinate (0,0), plotted from the non-motile *S. aureus* alone (Figure 3-3c; blue) as compared to those of *S. aureus* mixed with *P. aeruginosa* (Figure 3-3c; red) clearly illustrate the directed, extended motion of the non-motile bacteria in mixed culture. By comparing the MSD of *S. aureus* in the presence (Figure 3-3d; MSD assigned red) and absence (Figure 3-3d; MSD assigned blue) of *P. aeruginosa,* we found a distinct shift toward increased directed motility for the population in contact with *P. aeruginosa*. These trajectories are superdiffusive (Appendix B, Fig. B-6a,d), as has been postulated in the past for motion of motile bacteria driven by flagellar rotation [94].

For comparison, *S. aureus* was combined with non-motile *P. aeruginosa* strains PAO1Δ*motABCD* and PAO1Δ*flgE*. The strain PAO1Δ*motABCD* assembles flagella without rotational capabilities, and the strain PAO1Δ*flgE* does not assemble flagella. The measured motions of *S. aureus* in the presence of these bacteria did not noticeably deviate from those acquired in monoculture (Figure 3-3e,f; Appendix B, Figure B-3f,g, Figure B-7). Furthermore, fluorescence microscopy revealed that both mutant strains were incapable of localizing *S. aureus* to the air-liquid interface to the degree of wild-type *P. aeruginosa* PAO1 (Appendix B, Figure B-8), suggesting that the extended radius of activity of *S. aureus* is dependent on the swimming motility of *P. aeruginosa*.

Interactions between *P. aeruginosa* and *S. aureus* were also found to influence vertical migration of *S. aureus* as indicated by its increased presence in air-liquid

interface biofilms. Using fluorescence video microscopy at the top of the microchannel (~100 μm above the bottom), we observed *S. aureus* upward transport as the cells migrated into the imaging focal plane (Appendix B, Figure B-3d,e). In some instances, *S. aureus* became immobilized on the glass surface after upward movement. Collectively, these observations demonstrate that motile species influence physical motion and change the spatial distribution profile of non-motile *S. aureus* in a polymicrobial system.

Finally, using a combination of phase contrast and fluorescence microscopy, we observed the co-swimming behavior of *S. aureus* and *P. aeruginosa* in culture together. The two species were imaged swimming and attaching to glass surfaces together (Appendix B, Figure B-9). These videos qualitatively validate the quantitative differences seen in *S. aureus* motion in the presence of *P. aeruginosa* PAO1, which we attribute to them swimming together.

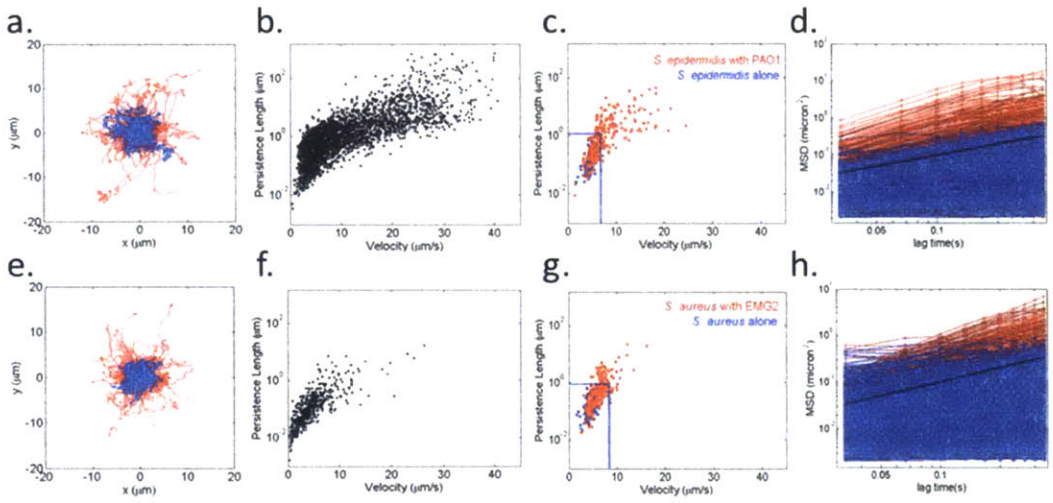

Figure 3-4. The acquisition of motility is not unique to the *S. aureus*, *P. aeruginosa* pairing, as similar results are achieved when mixing *S. epidermidis* strain DSM 20044 with *P. aeruginosa* and *S. aureus* with *E. coli* strain EMG2. (a,e) The traces of *S. epidermidis* on its own (blue) and *S. epidermidis* in the presence of *P. aeruginosa* (red) (a) or *S. aureus* on its own (blue) or when mixed with *E. coli* (red) (e) are shown, with all traces re-centered to the coordinate (0,0). Traces of the motile species, *P. aeruginosa* (b) and *E. coli* (f) respectively, shown as persistence length vs. velocity plots. (c,g) Traces of non-motile bacteria on their own (blue) or in the presence of a motile species (red), shown as persistence length vs. velocity plots. In (c) the non-motile species is *S. epidermidis*, and the motile species is *P. aeruginosa*, whereas in (g) the non-motile species is *S. aureus* and the motile species is *E. coli*. In both cases, there is a set of trajectories of the non-motile bacteria in the presence of motile bacteria with persistence lengths up to several orders of magnitude larger than those of the non-motile bacteria on their own. (d,h) The MSDs of all trajectories for *S. epidermidis* and *S. aureus* in the presence and absence of *P. aeruginosa* and *E. coli* respectively, using the same color code. In both cases, increased motility is seen with the non-motile bacteria in the presence of a motile species.

To test if the ability to borrow exogenous motility from swimming bacteria is more broadly applicable to other non-motile species, we performed similar experiments with *P. aeruginosa* and *Staphylococcus epidermidis* strain DSM 20044. When *S. epidermidis* was mixed with *P. aeruginosa* wild-type PAO1, the measured *S. epidermidis* trajectories also resulted in directed motility, larger persistence lengths, and increased velocity as compared to *S. epidermidis* alone (Figure 3-4a-d, Appendix B, Figure B-5b, Figure B-3h). In addition, flagellated *E. coli* EMG2 influenced *S. aureus* in a similar manner observed for *P. aeruginosa* (Figure 3-4e-h; Appendix B, Figure B-5c, Figure B-3i). Collectively, these data support a generalized mechanism for translocation among Staphylococcal species via interaction with flagellated bacteria.

Since bacteria have a number of polysaccharides and adhesins that influence physical interactions with their environment, we considered the possibility that his phenomenon is due to non-specific interactions between the species investigated. As a proxy for Staphylococcal cells, we mixed *P. aeruginosa* with 1 μm carboxylated fluorescent beads and examined the resulting air-liquid interface biofilms. We observed an increased accumulation of fluorescent beads incorporated into a *P. aeruginosa* biofilm at the interfacial region, revealing that electrostatic interactions between *P. aeruginosa* and the carboxylated beads promote the stowaway phenomenon also observed for Staphylococcal cells (Appendix B, Figure B-10). Furthermore, video microscopy confirmed the interactions between *P. aeruginosa* and the carboxylated beads, where beads acquired motility from swimming *P. aeruginosa* (Appendix B, Figure B-11).

3.3.3 Non-motile bacteria can also borrow motility in semi-solid medium

Opportunistic pathogens, such as *P. aeruginosa* and *S. aureus*, often colonize soft tissues and food sources. Hence, as a complement to our investigation in liquid environments, we observed the translocation of *S. aureus* through a semi-solid soft agar matrix to synthetically mimic biological tissues in both the presence and absence of *P. aeruginosa*. Motility assays were performed with < 0.3% agar to facilitate swimming behavior through water filled pores in the agar matrix. Using *S. aureus* expressing GFP, fluorescence microscopy revealed *S. aureus* 1 cm beyond the initial inoculation site in the presence of *P. aeruginosa* (Figure 3-5), whereas *S. aureus* inoculated alone remained within the immediate vicinity of the inoculation site.

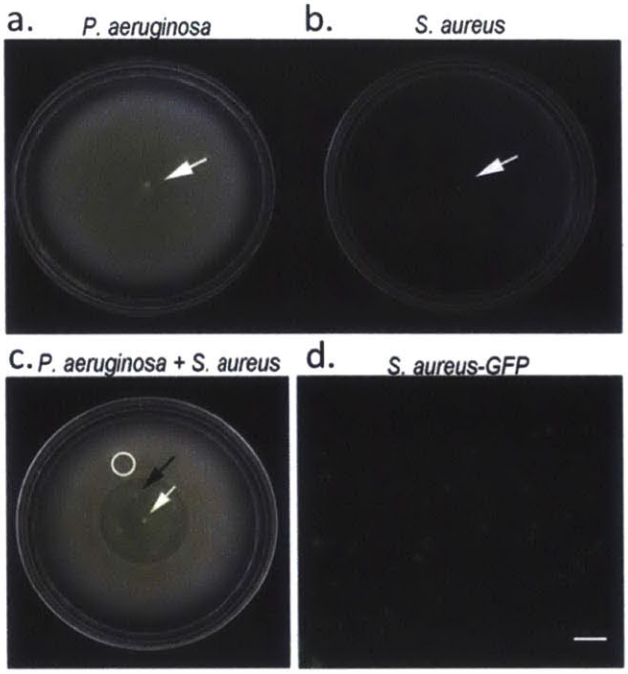

Figure 3-5. *P. aeruginosa* enhanced migration of *S. aureus* within a semi-solid matrix. (a) *P. aeruginosa* and (b) *S. aureus* RN4220 expressing GFP after 36 h post inoculation in 0.3% agar motility plates. *P. aeruginosa* was capable of migrating in a radial pattern from the center point of inoculation (a, white arrow), whereas *S. aureus* (b, white arrow) remained localized to the inoculation site. (c) Inoculation sites of *P. aeruginosa* (white arrow) and *S. aureus* (black arrow) in the same motility plate 36 h post inoculation. Separate inoculation sites for each strain were selected to encourage growth in the agar without immediate competition between the two strains. Agar samples were excised at 1 cm (white circle) beyond the *S. aureus* inoculation site. (d) The excised agar was screened for the presence of GFP expressing *S. aureus.* Scale bar represents 5 μm.

3.4 Materials and Methods

3.4.1 Strains and growth conditions

Staphylococcus aureus UAMS-1, *Staphylococcus aureus* RN4220 pALC2084 expressing GFPuv[95], *Staphylococcus epidermidis* DSM 20044, *Pseudomonas aeruginosa* PAO1, PAO1Δ*motABCD*, PAO1Δ*flgE* and *Escherichia coli* EMG2 were inoculated in LB medium and grown overnight at 37 °C. Each strain was then sub-cultured to a minimal OD of 0.8 for all experiments. All wild-type strains without selection requirements were grown in LB (BD Biosciences). PAO1 with the plasmid pBBR1MCS5-eGFP was grown in LB supplemented with 30 μg/ml of gentamicin (Sigma). EMG2 with the plasmid pBBR1MCS5-eGFP was grown in M63-glucose medium[96] supplemented with 5 μg/ml

of gentamicin. RN4220 with plasmid pSK236-GFPuv was grown in LB supplemented with 10 μg/ml of chloramphenicol. Mannitol Salt Agar (Sigma) for the selection of *S. aureus* from air-liquid interface biofilms was prepared according to the manufacturer's instructions. UAMS-1 and *Staphylococcus epidermidis* were stained with the gram-positive specific dye hexidium iodide (Molecular Probes) at a final concentration of approximately 15 μg/ml.

3.4.2 Air-liquid interface biofilm assays

P. aeruginosa PAO1 and *S. aureus* UAMS-1 in exponential phase were diluted to 10^6 or 10^8 colony-forming units (CFU) per ml in LB medium. For polymicrobial cultures, cells were mixed at a ratio of 1:1. 150 μl of culture was added per well to a sterile polystyrene microtitre plate (BD Falcon) and allowed to equilibrate undisturbed for at least 1 hour before adding inserts. Glass or polydimethylsiloxane (PDMS; Sylgard 184; Dow Corning, MI, USA) inserts (8mm x 5mm x 1mm) were aseptically placed into each well for biofilm growth. The plates were maintained at ambient temperature for 24 h. At the end of this time point, inserts were removed for analysis. Crystal violet staining of plates and inserts were performed as described previously[97]. Fluorescence images of air-liquid interface biofilms were acquired with a Zeiss Axio Observer Z1 microscope using a 100x/1.4 NA oil-immersion objective. PAO1 was visualized by eGFP expression. UAMS-1 cells were selectively stained with hexidium iodide before imaging. To quantify the composition of *S. aureus* in air liquid interface biofilms, cells were harvested via cell scraping. Collected cells were resuspended in 1 ml of LB medium and serially diluted for plating on selective mannitol salt agar. The average concentration of cells (CFU/ml) for three independent biological replicates was plotted with GraphPad Prism (GraphPad Software, San Diego, CA, USA, http://www.graphpad.com/). For biofilm assays with fluorescent beads, *P. aeruginosa* was inoculated as described above with the addition of carboxylated, polystyrene beads 1 μm in diameter (Invitrogen) diluted 1/1000.

3.4.3 Scanning electron microscopy (SEM)

For SEM analysis, polymicrobial cultures of PAO1 and UAMS-1 were prepared at a 1:1 ratio in LB and 150 μl of culture was added per well to a sterile polystyrene microtitre plate. The polymicrobial mixture was equilibrated for 1 hour at ambient temperature followed by the addition of a PDMS vertical insert. The plates were maintained at ambient temperature for a minimum of 2 hours to allow for initial attachment at the air-

liquid interfacial region. The vertical inserts were then fixed overnight in a 2% glutaraldehyde solution in PBS, pH 7.4, then washed with PBS and dehydrated in baths of increasing ethanol concentration (50, 70, 80, 90, 95, 99, 100 % ethanol, 5 min each). Ethanol was then exchanged with hexamethyldisilazane (HDMS, 2 baths of 5 minutes) and air-dried overnight. The samples were mounted on carbon tape and sputter coated with a gold layer (approximately 10 nm). Imaging was performed on a JOEL 6010LA scanning electron microscope.

3.4.4 Depth of field/bacteria number assays

Chamber slides were made by attaching 18x18 mm coverslips to 24x60 mm coverslips with Parafilm to create a chamber about 100 μm in depth. Carboxylated, polystyrene beads 1 μm in diameter (Invitrogen) were diluted 1/1000 in LB from the stock solution and placed into the chambers. The chambers were sealed with vacuum grease and imaged on a Zeiss Axio Observer Z1 microscope with a 40x/0.75 NA objective, and a cMOS camera (Hamamatsu). Ten images were taken at three locations per slide in three different slides, and an average number of beads in focus per field of view was calculated. This was used to calculate a depth of field by figuring out what volume the field has based on the known concentration of beads in the solution and the number of beads in the field of view, as previously described[98].

3.4.5 Semi-solid agar motility assay

Agar motility plates were prepared as described elsewhere[99]. For single species motility assays, *P. aeruginosa* PAO1 and *S. aureus* RN4220 expressing GFPuv were inoculated into the agar center with a sterile pipette tip. Single species assays were used to confirm swimming and non-motile phenotypes of PAO1 and RN4220, respectively. For polymicrobial motility assays, PAO1 was inoculated once in the center of the plate surrounded by 4-5 inoculation sites for RN4220 1 cm from the PAO1 inoculation site. This inoculation strategy was employed to allow each strain to establish growth within the agar medium without immediate competition between strains. Motility plates were placed at 37°C for a minimum of 36 hours. A 5mm biopsy punch was used to carefully isolate agar plugs 1 cm from *S. aureus* RN4220 inoculation sites (equivalent to 2 cm from PAO1 inoculation site). Agar plugs were placed on a 24x60 mm coverslip for imaging fluorescent *S. aureus*. All images for were acquired with a Zeiss LSM 510 Meta Confocal using a 100x/1.4 NA oil immersion objective.

3.4.6 *Cell and bead tracking assays*

Slides for tracking were made by attaching 18x18 mm coverslips to 24x60 mm coverslips using Parafilm to create a chamber ~100 μm high. Solutions of bacteria, diluted to $1x10^8$ cells/ml for each species were pipetted into the slides, which were then sealed with vacuum grease. The slides were then immediately imaged, using a Zeiss Axio Observer Z1 microscope with a 40x/0.75 NA objective, and a CCD camera (Allied Vision Technologies) to take 30 second long videos at 30 frames per second. Bacteria were tracked in two dimensions using publicly available MATLAB codes (Kilfoil Group, http://people.umass.edu/kilfoil/downloads.html) with some modification. Velocities and persistence length were calculated using code written in-house. Bead/bacteria solutions were prepared in a similar fashion with, stock solution of 1 μm diameter, carboxylated beads (Invitrogen) diluted to 0.33 v/v%. These were imaged and tracked as described for the bacteria mixtures. To measure static error, slides containing just the non-motile species were covered with aluminum foil (to avoid photobleaching) and left to sit for two hours to allow all bacteria to settle to the bottom of the chamber before imaging (Appendix B.4).

3.4.7 *Velocity calculation*

The average velocity was calculated using the following method:

$$\overline{v} = \frac{1}{t} \cdot \frac{1}{N-1} \sum_{i=1}^{N-1} \left| r_{i+1} - r_i \right| \qquad \text{(Equation 3-1)}$$

where t is the time between frames or the inverse of the frame rate, N is the number of points in the trajectory, and r is the position of the bacteria in the xy plane at a point in the trajectory.

3.4.8 *Persistence length calculation*

Persistence length of each trajectory was calculated using the following equation:

$$\left\langle \cos\theta_l \right\rangle = e^{(-l/L_p)} \qquad \text{(Equation 3-2)}$$

where l represents the distance traveled along the curve, $\cos\theta_l$ is the angle between tangents to the path at points distance l apart, L_p is the persistence length, and a time average was used, as will be described. The persistence length was fit to only the positive $\langle\cos\theta\rangle$ values of a trajectory, only for lag times for which there were at least

three points to average, and only on trajectories for which there were at least three lag times to fit to.

To calculate a persistence length using discrete time points, a few assumptions were made. The first that is the tangent to the curve at any point between two time points is parallel to the ray connecting the two points. Second, statistically there should be a point between r_i and r_{i+1} that is separated by the distance $n\bar{v}\lambda$ from a point between r_{i+n} and r_{i+n+1}, where r represent the discrete points, n is the number of time lags, $\bar{v}$ is the average velocity along the trajectory and λ is the time between frames (1/30 of a second in this case). This allowed us to then calculate a persistence length using points a known number of lag times apart, by relating the lag time to the length traveled along the curve, and using the law of cosines to calculate the angle between tangents. A schematic is shown in Appendix B, Figure B-12. There were traces for which persistence lengths could not be calculated as the average of $\cos\theta$ dropped below 0 within 3 lag times, likely due to random motion or immobilization of cells on the glass surface. Since a persistence length could not be fit to the data, they are not shown in Figures 3-2a-b, 3-2e-f, 3-3b-c and 3-3f-g. However, we did calculate upper bound thresholds for the persistence lengths for these points, which are shown in Appendix B, Figure B-13. These bounds are linearly related to the velocity as they were approximated by $n_{drop}\bar{v}\lambda$ where n_{drop} indicates the point at which $\cos\theta$ dropped below zero, since this is approximately how far the bacteria could have traveled in that time step.

3.4.9 Co-swimming video microscopy

Slides were prepared as for the cell tracking assays. Combination phase-contrast and fluorescence microscopy were used to visualize and distinguish between the cell types. Videos were acquired using a Zeiss Axio Observer Z1 microscope with a 100x/1.4 NA oil immersion objective, and a CCD camera (Allied Vision Technologies) to take 30 second long videos at 30 frames per second.

3.5 Conclusions

The findings presented here quantitatively indicate that Staphylococcal species, classically defined as non-motile, have altered motility patterns in the presence of flagellated *P. aeruginosa* and *E. coli.* Specifically, *P. aeruginosa* and *E. coli* function as microbial carriers for Staphylococcal stowaways and result in enhanced dispersal range in fluid and semi-fluid environments. This represents a novel mechanism of motility for the Staphylococcal species tested. Furthermore, this mechanism is distinct from surface associated movement, such as colony spreading, previously observed for *S. aureus* on agar surfaces[100].

Much work has focused on flagellar-mediated swimming motility to enable bacterial locomotion[101-103]. Despite the wealth of information regarding bacterial self-propulsion, the contributions of interspecies interactions are not well understood. In most natural environments, bacteria are part of polymicrobial communities[104-106]. The primary motivation of this work is to highlight multispecies effects on translocation and distribution of non-motile bacteria.

Based on our observations, we suspect that other non-flagellated species conceivably seize the opportunity to borrow motility from physical microbe-microbe interactions with flagellated bacteria. The concept of "hitchhiking" has been demonstrated for bacteria with eukaryotic partners on greater scales[107,108]. We found that this behavior could directly change the localization patterns of Staphylococci and open new niches for colonization of this opportunistic pathogen, as observed in biofilm formation at the air-liquid interface. Looking forward, such behavior could influence community diversity, microbial dispersal, and perhaps enhance transmission of non-motile pathogenic strains. From a clinical perspective, our observations have far reaching implications on how non-motile bacteria disseminate. Coupled with traditional modes of transmission, such as direct contact with infected bodily fluids or air-borne droplets, riding with flagellated bacteria could enable dispersal of non-motile pathogens from localized polymicrobial infections to other tissues or enhance distribution within contaminated food sources. Ultimately, we envision that the results of our study will encourage new investigations to consider the effects of polymicrobial interactions to characterize distribution of non-motile bacteria.

CHAPTER 4

Conclusions and Outlook

This thesis presents work in which single particle tracking was used to elucidate the physical properties and dynamics of bacterial systems. The first project developed a framework for understanding spatiotemporal differences in biofilm physical properties and for assessing the presence of fluid-filled channels within a biofilm. The second project involved tracking bacteria to measure how non-motile species acquire motility by riding on their motile neighbors. Both projects provide a base for a number of other potential projects.

4.1 Particle Tracking of Beads to Understand Biofilm Properties and Life Cycle

In Chapter 2, a methodology was developed to methodically measure the physical properties of bacterial biofilms by probing them with different size and charges of polystyrene microparticles. The goal of developing this method is to provide a basis for providing comparable measurements of biofilm physical properties. The ability to

provide spatiotemporal resolution and the minimal perturbation to the biofilm allow for multiple types of experiments to better understand biofilms.

As discussed in Chapter 1, the best characterized biofilm system is that of *P. aeruginosa*, an opportunistic pathogen. The biofilms of *P. aeruginosa* are known to contain several major polysaccharides, alginate, which is unimportant in the biofilm development of lab strains, Pel and Psl. Psl polysaccharide is required for both cell adhesion to a surface, and structural support of a mature biofilm and Psl deficient strains have difficulty forming biofilm due to lack of adhesion[109]. Pel polysaccharide maintains structure of the biofilm without playing a major role in adhesion, and is required to produce normal biofilm morphology[23,110,111]. Several groups have studied the effects of knocking out each polysaccharide individually or in concert and have observed different morphological results based on the bacterial strain used. In one strain, the *pel* gene knockout was observed to have morphology more similar to wild type than the *psl* gene knockout, whereas the double knockout was the most morphologically different[23]. In addition, it has been shown that the type of growth condition (flow vs. solid medium) may impact the way in which absence of a particular gene changes biofilm morphology[24].

By applying the methodology developed in chapter 2 to genetically varied *P. aeruginosa* it may be possible to collect the structural data to explain the way in which colony morphologies change due to genetic changes. Observing how these differences manifest over time or in response to growth in either static conditions or under flow, the specific mechanisms by which the different polysaccharides provide structure to the biofilm could be determined. Alginate is thought to be a non-essential component of the biofilm matrix in laboratory *P. aeruginosa* strains, as measured by bulk tests of biofilm integrity (height, visual heterogeneity, and mass)[21]. These tests cannot account for the possibility that an alginate knockout biofilm could seem externally similar to the wild-type strain, but have microscale internal structural differences. If the biofilms are indeed structurally similar, then wild-type and alginate knockouts would have the same measured physical properties via particle tracking. Using the developed technique it would be possible to directly compare the matrix density, pore size, and heterogeneity to the corresponding wild-type strain to determine the internal effects of this deficit.

Psl deficient *P. aeruginosa* strains were shown to have difficulty adhering to surfaces and forming biofilms under flow conditions, though they can form biofilms on a solid medium. Thus, it would make sense to analyze four different conditions for understanding the internal structure of Psl deficient *P. aeruginosa*: *P. aeuroginosa* biofilm grown in static culture, *P. aeuroginosa* biofilm grown in a microfluidics chamber, and *P. aeuroginosa* Δ*psl* biofilm grown in static culture and in a microfluidics chamber. By controlling for both strain and growth environment flow rates, it is possible to specifically probe the changes in structure induced by Psl deficiency in either condition as compared to a native strain biofilm.

Using a similar methodology as for the *psl* knockouts, it may be possible to assess the differences between native *P. aeruginosa* and *pel* knockout strains. These strains form biofilms, but biofilm maturation is affected, so it would be particularly interesting to measure properties in a temporal fashion to see at which point in development the change in structure occurs. If *P. aeruginosa* has particular internal structural formations, these will likely be lost with a *pel* knockout, and the correlation between structure and its advent in a biofilm's existence can be determined. To measure what structural differences exist and when they arise, the methodology from Chapter 2 could be applied to *P. aeruginosa* and *P. aeruginosa* Δ*pel* strains at different times in development.

The methodology described in Chapter 2 may also be useful for better understanding biofilm dispersal. Dispersal is a normal part of the biofilm life cycle in which bacteria are released from the biofilm into the surrounding. Many materials are known to cause dispersal of biofilms, by which the bacteria release large quantities of cells into the surrounding environment [112]. One of these materials, *cis*-2-decenoic acid, has been added externally to biofilms of multiple species to induce visible dispersal of bacteria from preformed biofilms as measured microscopically and morphologically[113]. The dispersal of biofilms may be in part due to internal structural changes induced by adding these agents and thus comparing the structure of biofilms treated with such agents to the native biofilms grown under the same conditions might provide insight into the effects of these agents.

4.2 Further Investigation of Interspecies Interactions

Chapter 3 presents evidence that some species of non-motile bacteria can gain motility by riding on their motile neighbors. While this is an important observation, there are many open questions as to the general applicability of the result and as to specifics of the interaction. All the measured pairs in Chapter 3 consist of a non-motile gram-positive species mixed with a motile gram-negative species. Therefore it is possible that the effect is limited to such pairs, even though many clinically relevant pairings are gram-positive/gram-negative. To further explore this, it would make sense to perform similar experiments on pairings that do not fall into this pattern, though depending on the choice, it may be difficult to differentially color the bacteria for imaging purposes.

The interspecies interaction is not entirely specific, as similar results are seen when charged microbeads are introduced with bacteria. However, there are likely some surface molecules presented by the bacteria that mediate the interaction. It would be possible to further understand this by choosing a non-motile/motile pair for which this interaction holds and to then specifically remove certain surface molecules by genetic modification. The experiments presented in Chapter 3 could be performed on the modified pair to determine if the altered molecule is important for the interaction. It should be noted, however, that the large number of potential surface molecules to alter may prevent this from adding useful insight.

It may be of use to figure out how to disrupt this interspecies interaction, as it could provide insight into preventing complex, mixed-species infections as are sometimes be seen with medical implants. Since the interaction may be at least partially charge-mediated, increasing the salt concentration of the medium may be a way of mitigating the interaction. While this would not be a medically-relevant solution, it would be a step to better understanding the interaction.

APPENDIX A

Supplementary Information for Chapter 2

A.1 Static Error Measurements

Table A-1. Static error for different bead types.

Bead Type	Color	Size (nm)	Static Error (μm^2)
PEGylated	red	1110±46	$2.4x10^{-5}$
PEGylated	green	2020±16	$4.5x10^{-5}$
carboxylated	green	516±11	$4.3x10^{-4}$
carboxylated	red	1100±35	$2.7x10^{-5}$
carboxylated	green	2000±40	$4.1x10^{-5}$
aminated	green	1100±35	$2.9x10^{-5}$

A.2 Conversion between MSD and Apparent Creep

The conversion from our scaled 2-dimensional MSDs in (μm^3) to creep in Pa^{-1} is about 600 as shown below:

$$J(\tau) = \frac{3\pi d}{4k_B T}\left\langle \Delta r^2(\tau) \right\rangle \qquad \text{(Equation A-1)}$$

$$J(\tau) = Cd\left\langle \Delta r^2(\tau) \right\rangle \text{ where } C = \frac{3\pi}{4k_B T} \qquad \text{(Equation A-2)}$$

Plugging in the known values to find C:

$$C = \frac{3\pi}{4k_B T} = \frac{3\pi}{4\left(1.38*10^{-23}\frac{J}{K}\right)(295.5K)} = \frac{3\pi}{4\left(1.38*10^{-23}\frac{kg\cdot m^2}{s^2}\right)(295.5K)} \cdot \frac{10^{-18}m^3}{\mu m^3} = 577.8\frac{1}{\mu m^3 \cdot Pa}$$

A.3 Approximation of Debye length in LB

LB is a bacterial growth medium that consists of 10 g/L NaCl and 15 g/L protein products in water, so NaCl is the dominant ionic species.

$$\lambda = \left(\frac{F^2}{\varepsilon_r \varepsilon_0 RT}\sum_{i=1}^{n} z_i^2 C_{i\infty}\right)^{-1/2} \qquad \text{(Equation A-3)}$$

F = Faraday constant =9.65*10^4 C/mol

R = molar gas constant = 8.3145 J/(K*mol)

z_i is charge of ion (+1 for Na, -1 for Cl)

$C_{i\infty}$= concentration of ion in bulk = 0.17 mol/L

ε_r = dielectric constant of water ~80

ε_0 = permittivity of free space = 8.85*10^{-12} Farads/m

Plugging in yields: λ = 7.4*10^{-10} m ~ 1 nm (<< particle diameter).

The Debye length is much less than the diameter of the beads, and thus the particles themselves should not be interacting with one another, and only local charge interactions are important.

APPENDIX B

Supplementary Information for Chapter 3

B.1 Calculation of approximate sedimentation rate of bacteria

First we perform a force balance around the bacteria and apply Newton's second law:

$$F_{net} = F_d + F_b - F_g = ma \qquad \text{(Equation B-1)}$$

where F_{net} is the net force around the bacteria, F_d is the drag force on the bacteria, F_b is the buoyancy force applied by the liquid, F_g is the force due to gravity, m is the mass of the bacterium, and a is the acceleration of the bacteria. When terminal velocity is reached, acceleration is equal to zero, so this becomes:

$$F_{net} = F_d + F_b - F_g = 0 \qquad \text{(Equation B-2)}$$

The F_b and F_g terms are easy to define at all times:

$$F_g = \rho_{bac} V_{bac} g \quad \text{(Equation B-3)}$$

$$F_b = \rho_{med} V_{bac} g \quad \text{(Equation B-4)}$$

where ρ is density, V is volume, and g is the acceleration due to gravity. The drag term depends on the flow type. Given, the small size of the bacteria, we are likely in a creeping flow regime (where Reynold's Number - Re, is much less than 1). We can check this by backing out the velocity the bacteria would need to achieve in order for this to not be the case.

$$\mathrm{Re} = \frac{vD}{\nu} \quad \text{(Equation B-5)}$$

where Re is the Reynold's number, v is the bacteria velocity, D is the diameter of the bacteria, and ν is the kinematic viscosity of the fluid. We know that the bacteria diameter is ~10^{-6} m, we want a Reynold's number of 0.01 or less, and that the kinematic viscosity of liquid medium at room temperature is ~10^{-6} m^2/s. Therefore, for Re to remain under 0.01, the velocity of the bacteria needs to be under ~1 cm/s (.01 m/s). The fastest motile bacteria we tracked move at ~50 μm/s, which is several orders of magnitude less than this. Therefore, the creeping flow assumption is reasonable. Creeping flow allows us to use Stoke's law to approximate the drag force as follows:

$$F_d = 6\pi\mu v R \quad \text{(Equation B-6)}$$

where μ is the dynamic viscosity, v is velocity, and R is the radius of the bacteria.

Thus to plug in and solve for v_t, the terminal velocity we get:

$$F_{net} = 6\pi\mu v_t R + \rho_{med} V_{bac} g - \rho_{bac} V_{bac} g = 0 \quad \text{(Equation B-7)}$$

We know the radius of bacteria (~0.5 μm), the volume of the bacteria (~0.52*10^{-18} m^3), the kinematic viscosity of the fluid medium (~0.899*10^{-3} kg/m/s), g (-9.8 m/s^2), ρ_{med} (1025 kg/m^3), and ρ_{bac} (~1050 kg/m^3). Putting everything together yields a terminal velocity of about 55 μm/hour in the downwards direction.

A bacterium reaches ~2/3 of terminal velocity at v_t/a_0 where a_0 is the acceleration at time 0, when v=0. To calculate a_0, we use Supplementary Equation 2, with F_d=0. Plugging in the other known values yields a_0~.24 m/s^2, so the bacteria will reach terminal velocity in well under 1 second, and we can assume they are at or near this velocity for most of the experiment.

B.2 Supplementary Tables

Table B-1. Depth of field calculations and approximated bacteria numbers.

Coordinate	Size (μm)
x (measured)	209.664
y (measured)	159.744
z (measured)	3.472

Sample	Concentration (per mL)
bead stock, 1/1000	$2.7*10^7$
bacteria (known initial CFU)	$1.0*10^8$

Sample	Number in Field of View (FOV)
beads in FOV (measured)	3.14
bacteria in FOV (expected)	11.63

B.3 Supplementary Figures

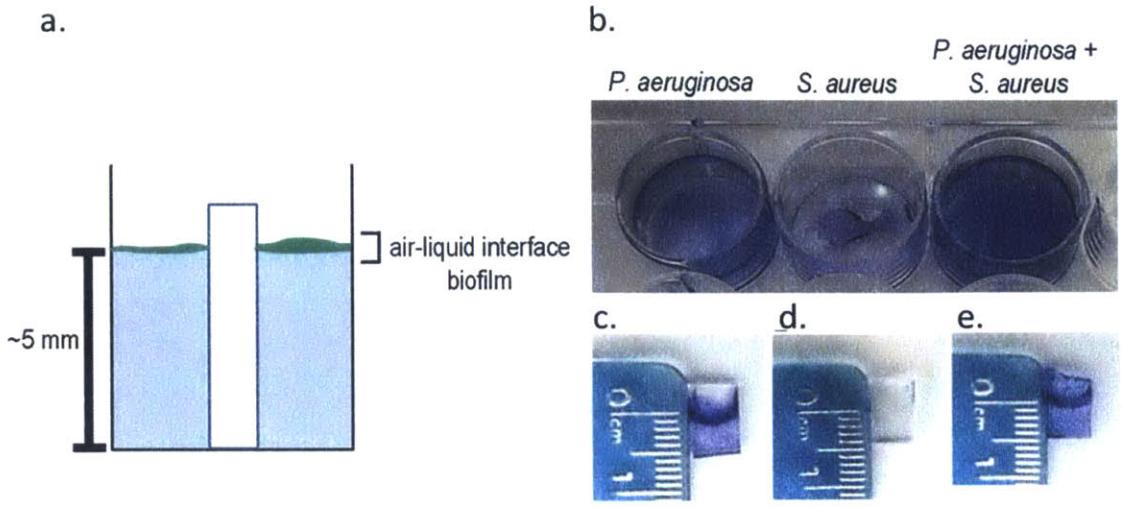

Figure B-1. Biofilm formation for *P. aeruginosa* and *S. aureus* in mono- and mixed species cultures. (a) Scheme of glass or PDMS inserts used for analysis of air-liquid interface biofilm formation in 96 well microtitre plates. (b) Crystal violet stain of biomass after 24 h of static growth at ambient temperature. Crystal violet stain of biomass on glass inserts with monocultures of *P. aeruginosa* (c), *S. aureus* (d), and polymicrobial cultures of *P. aeruginosa* and *S. aureus* (e).

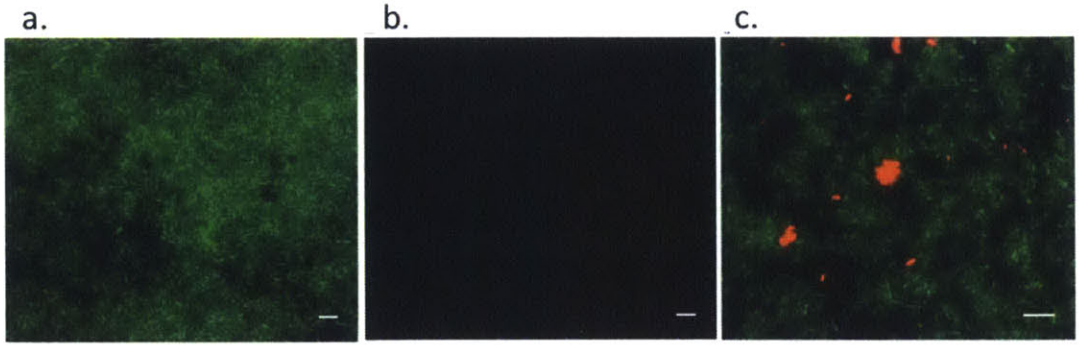

Figure B-2. Biofilm formed on PDMS inserts. Microscopic observations of *P. aeruginosa* (a) and *S. aureus* (b) and mixed culture (c) at the air-liquid interface of PDMS vertical inserts after 24 hours. Scale bars represent 5 μm.

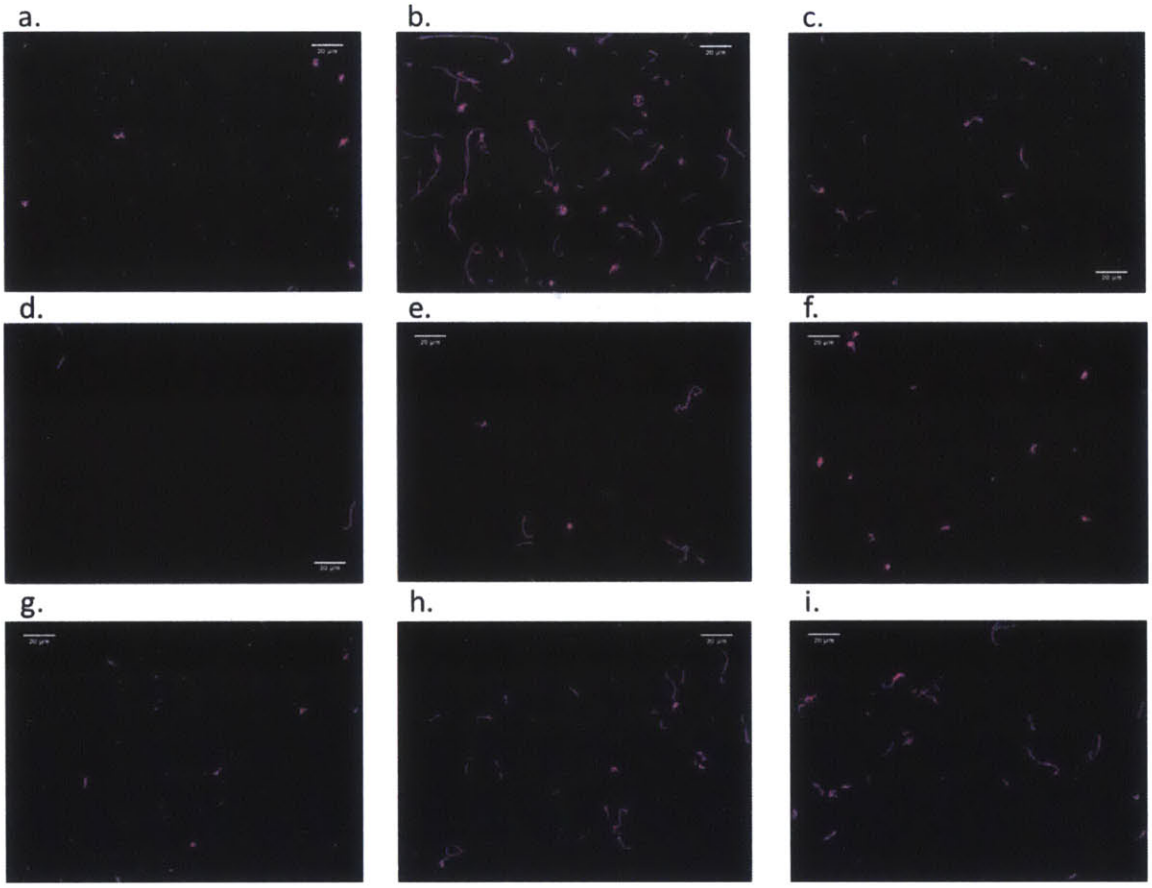

Figure B-3. Still images from the ends of bacteria trace videos. (a) Traces of *S. aureus* on its own. (b) Traces of *P. aeruginosa* on its own. (c) Traces of *S. aureus* in the presence of *P. aeruginosa*, at the bottom of a chamber slide. (d) Traces of *S. aureus* in the presence of *P. aeruginosa*, at the top of a chamber slide. (e) Traces of *S. aureus* in the presence of *P. aeruginosa*, at the top of a chamber slide, with evidence of flagellar rotation. (f) Traces of *P. aeruginosa* PAO1Δ*motABCD* on its own. (g) Traces of *S. aureus* in the presence of *P. aeruginosa* PAO1 Δ*motABCD*. (h) Traces of *S. epidermidis* in the presence of *P. aeruginosa.* (i) Traces of *S. aureus* in the presence of *E. coli*. All scale bars are 20 microns.

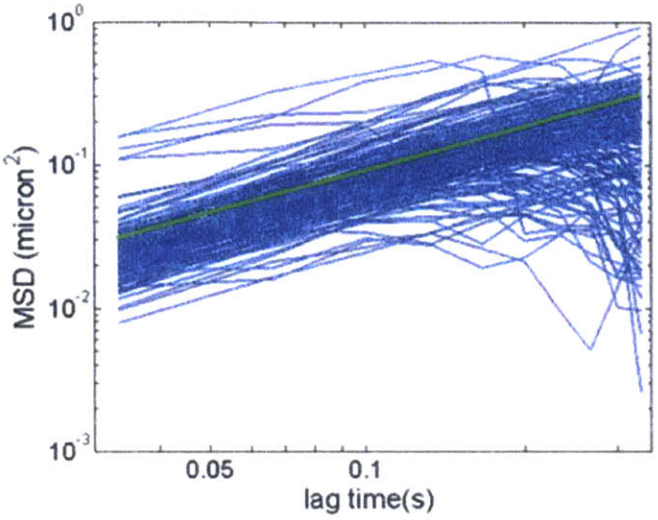

Figure B-4. The MSD of each individual trace of *S. aureus* for which we could calculate a persistence length is represented in blue. They are similar to the estimated MSD based on the diffusivity of similarly sized microparticles in liquid medium, represented in green.

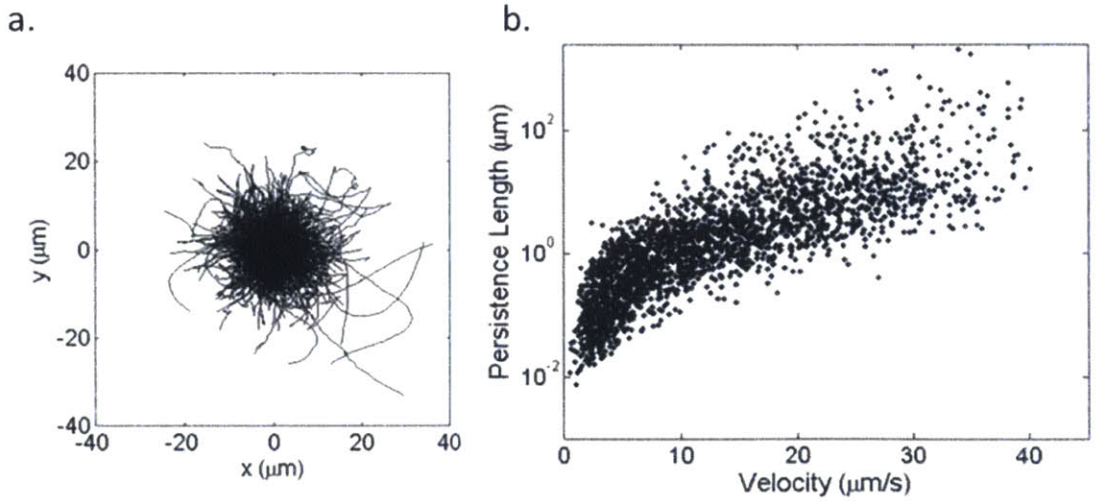

Figure B-5. Motility patterns observed for *P. aeruginosa* PAO1. (a) Motility traces of *P. aeruginosa* alone re-centered to begin at coordinate (0,0). (b) Individual trajectories of *P. aeruginosa* when mixed with *S. aureus* plotted on axes of persistence length vs. velocity.

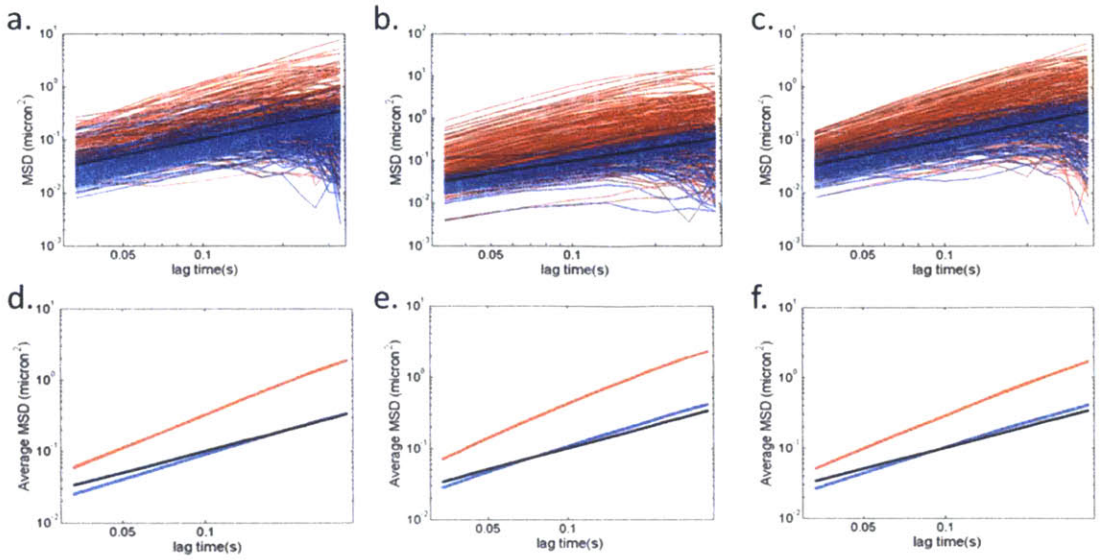

Figure B-6. MSDs of non-motile bacteria alone are diffusive, whereas they are superdiffusive in the presence of motile bacteria. (a) The MSDs of *S. aureus* alone (blue) and *S. aureus* mixed with PAO1 (red), shown with a line of slope 1 (black). The *S. aureus* alone appear to be diffusive (MSD with slope of 1), whereas a subset of *S. aureus* in the presence of *P. aeruginosa* appears to be superdiffusive (slope greater than 1). (b) The MSDs of *S. epidermidis* alone (blue) and *S. epidermidis* mixed with *P. aeruginosa* (red), shown with a line of slope 1 (black). The S. *epidermidis* alone appear to be diffusive (MSD with slope of 1), whereas a subset of *S. epidermidis* in the presence of *P. aeruginosa* appears to be superdiffusive (slope greater than 1). (c) The MSDs of *S. aureus* alone (blue) and *S. aureus* mixed with *E. coli* (red), shown with a line of slope 1 (black). The S. *aureus* alone appear to be diffusive (MSD with slope of 1), whereas a subset of *S. aureus* in the presence of *E. coli* appears to be superdiffusive (slope greater than 1). (d-f) The averaged population MSDs (red and blue) and a line of slope 1 (black) matching the traces shown in panels a-c respectively, with color coding matching those panels as well. These show that on average, the non-motile bacteria appear approximately diffusive, with a slope of 1, whereas the non-motile species in the presence of motile bacteria appear superdiffusive, with slope greater than 1. For all panels, the traces represented are only those for which we could calculate a persistence length, indicating that the bacteria were not immobilized to the glass slide.

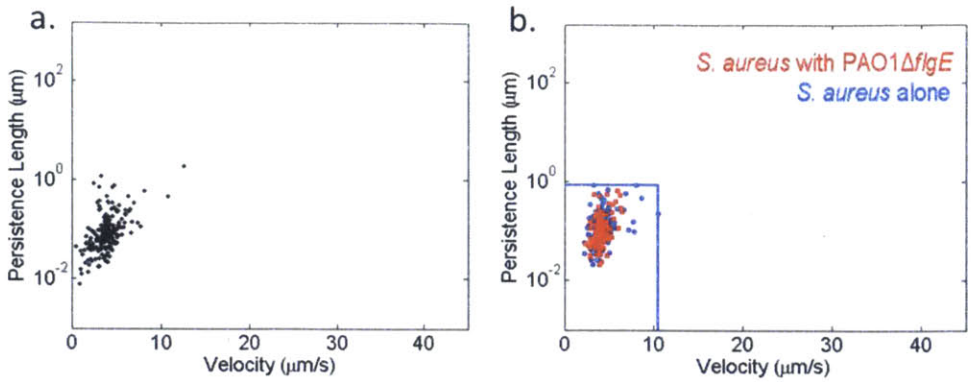

Figure B-7. The *P. aeruginosa* PAO1Δ*flgE* mutant strain does not influence the motility patterns of *S. aureus* when combined. (a) Individual trajectories of PAO1Δ*flgE* alone in culture exhibit smaller persistence lengths and velocities than *P. aeruginosa.* (b) The trajectories of *S. aureus* alone (blue), and of *S. aureus* in the presence of PAO1Δ*flgE* (red).

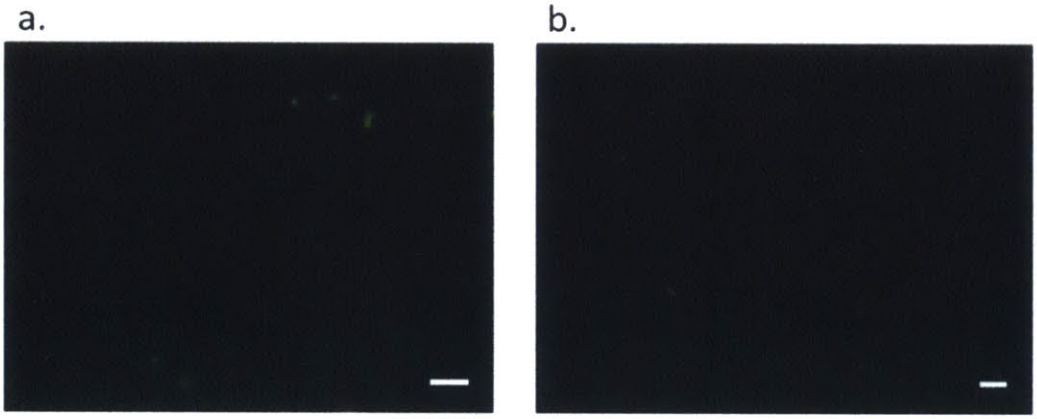

Figure B-8. *P. aeruginosa* without swimming motility does not facilitate polymicrobial biofilm formation at the air-liquid interface. (a) *P. aeruginosa* PAO1Δ*motABCD* and (b) PAO1Δ*flgE* after 24 hours of growth with *S. aureus.* Fluorescence images of the air-liquid interface region reveal only a few *P. aeruginosa* cells expressing GFP after 24 hours of static growth. Scale bars represent 5 μm.

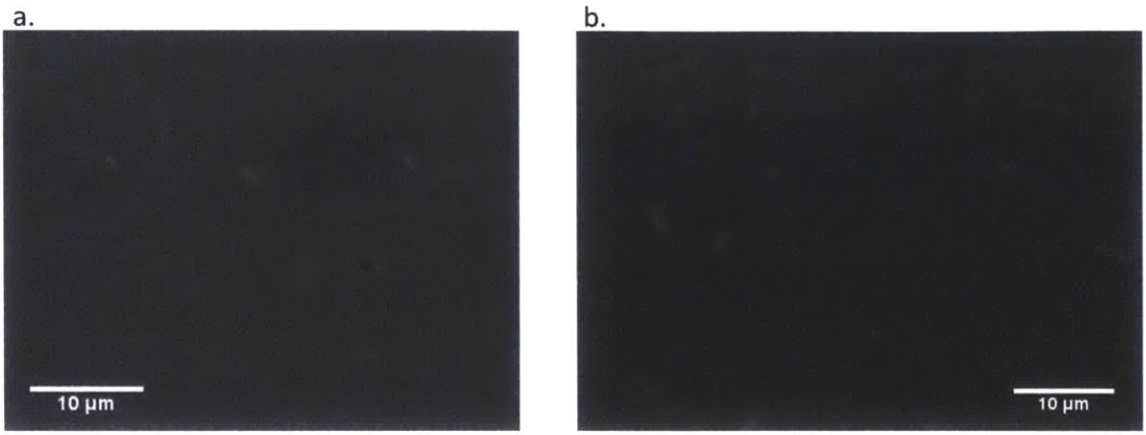

Figure B-9. Still images taken from phase constrast with fluorescence videos of *S. aureus* mixed with *P. aeruginosa*. In (a-b) co-localized S. *aureus* (black from phase-contrast) and *P. aeruginosa* (white from fluorescence) are seen. In the video, several of these pairs are in motion whereas others are stuck to the glass surface.

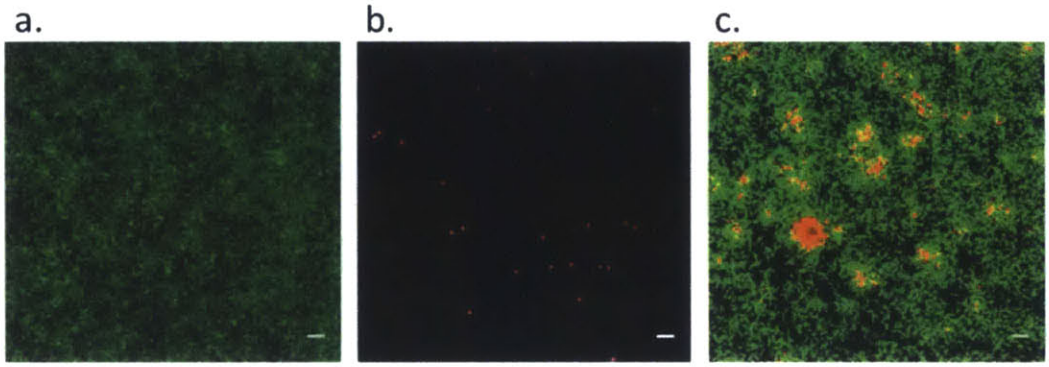

Figure B-10. *P. aeruginosa* can incorporate microscale beads into biofilm at the air-liquid interface. Microscopic observations of *P. aeruginosa* (a) and 1 µm carboxylated florescent beads (b) and mixed *P. aeruginosa* and beads (c) at the air-liquid interface of glass vertical inserts after 24 hours. Scale bars represent 5 µm.

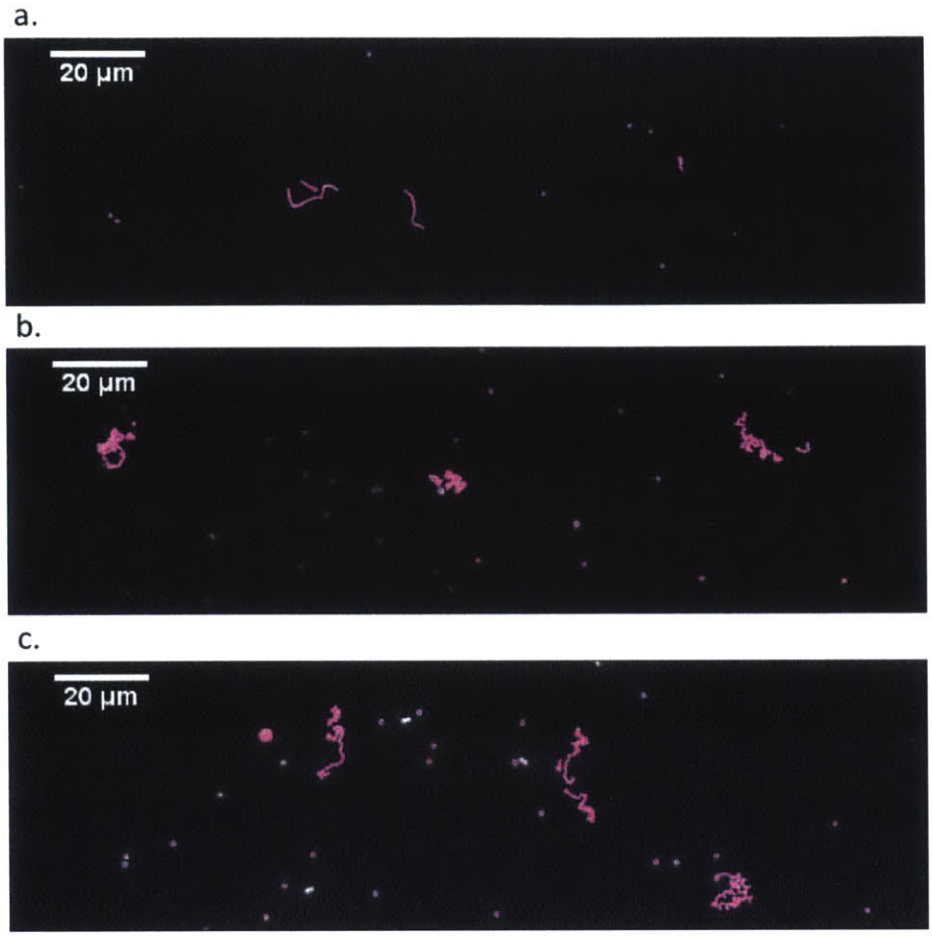

Figure B-11. Still images from the ends of bead trace videos. (a) Traces of beads at the bottom of a chamber, showing linear trajectories for beads in the presence of PAO1. (b) Traces of beads at the bottom of a chamber, showing a circular trajectory, again indicating acquired motion. (c) Traces of beads at the top of a chamber slide, showing beads settling upwards to the top, which would not happen with beads on their own, as well as a bead moving in a circular fashion, likely due to PAO1 flagellar spinning.

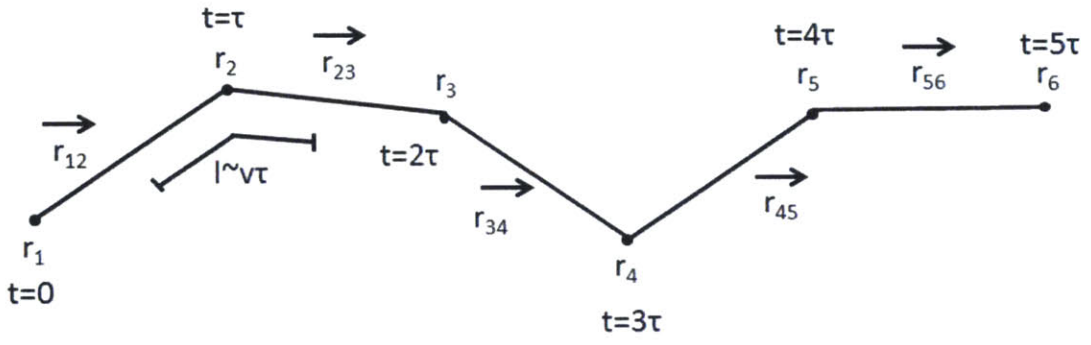

Figure B-12. A schematic representation of the methodology employed to calculate persistence length from cell traces.

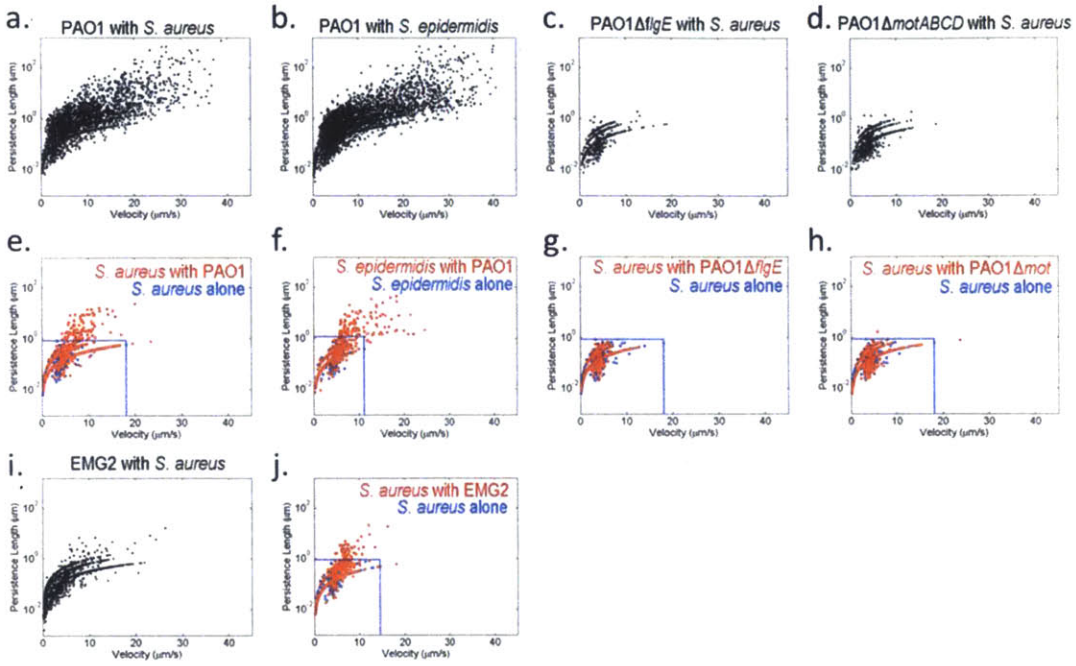

Figure B-13. Persistence length vs. velocity plots for all trajectories. (a-j) The trajectories of all traces acquired for all strains plotted on axes of persistence length vs. velocity. These data include upper bound thresholds of the persistence lengths for trajectories for which persistence length could not be calculated as the average of cosθ dropped below 0 within 3 lag times.

B.4 Static Error Measurements

The static error for the non-motile bacteria at the imaging conditions described in section 3.4.6 is 0.002 μm^2.

APPENDIX C

Other Techniques

C.1 Measuring Diffusivity and Partition Coefficient

We attempted to measure the diffusivity and partition coefficient of beads in biofilms using the technique described here. While it did not work well for the biofilms, given difficulties in determining a definite height and the lack of homogeneity, it may be useful for other systems. The experiment requires the experimenter to watch bead concentration change over time at one height in the biofilm after a bulk concentration is added to the media above it, as diagrammed in Figure C-1.

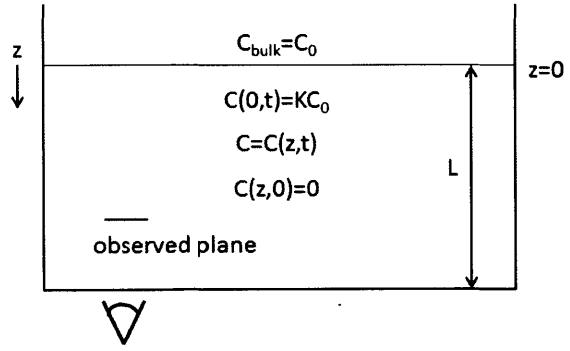

Figure C-1. A diagram of the diffusion experiment setup.

Several assumptions are made in order to find an analytical solution to fit the data acquired in this fashion, including a bulk condition at the fluid/gel interface and symmetry of the system such that diffusion only occurs in the z direction. We also assume no flux of beads through the glass surface at the bottom of the gel, and that before introduction of the bead solution above the gel, it contains no beads. Using the finite Fourier transform method, we can find an analytical solution to the concentration profile given these conditions, where θ is the nondimensionalized concentration C/C_0, Z is the nondimensionalized z coordinate (z/L), and τ is nondimensionalized time (tD/L^2):

$$\theta(Z,\tau) = K - 2K\sum_{n=0}^{\infty}\frac{1}{\lambda_n}(e^{-\lambda_n^2\tau})\sin(\lambda_n Z) \qquad \text{(Equation C-1)}$$

$$\lambda_n = \pi\left(n+\frac{1}{2}\right) \qquad \text{(Equation C-2)}$$

To elaborate further on the assumptions, a bulk condition at the gel/fluid interface implies that the beads moving into the gel do not deplete the bulk. The bulk fluid in these experiments takes up more than 10 times the volume of the gel, which means that in the case of a partition coefficient of order 1, the bulk concentration will remain within 10 percent of its original value when steady state is reached. Bead flux into the biofilm could lead to a boundary layer at the gel/media interface, such that the bulk is depleted locally. The flux into the gel is largest at $t=0^+$, as this is the point at which the concentration gradient in the gel is largest. By examining the fluxes for this limiting case, we can approximate how far the system deviates from bulk. Mass balance at the interface tells us that diffusive flux into the interface is equal to the diffusive flux out of it as follows, where D_1 is the diffusion constant in the bulk medium, D_2 is the diffusion constant in the biofilm, K is the partition coefficient, C_{z-} is the concentration on the medium side of the interface, C_0 is the bulk concentration, and we know C=0 inside the biofilm due to our initial conditions:

$$D_1(C_0 - C_{z-}) = D_2(KC_{z-}) \qquad \text{(Equation C-3)}$$

If we rearrange this to solve for C_{z-}/C_0, we yield the following relationship:

$$\frac{C_{z-}}{C_0} = \frac{1}{1+K\dfrac{D_2}{D_1}} \qquad \text{(Equation C-4)}$$

Therefore, if we assume that the bulk condition holds if C_z/C_0 is greater than 0.9, then KD_2/D_1 must be of order 10^{-1} or less. While we do not know whether this is true a priori, the assumption can be validated based on experimental results. Finally, we note that due to the symmetry of the system, diffusion will occur only in the z-direction.

Taking these assumptions into account, the concentration over time in a particular location can be described by the following nondimensionalized conservation equation, where θ is the nondimensionalized concentration C/C_0, Z is the nondimensionalized z coordinate (z/L), and τ is nondimensionalized time (tD/L^2):

$$\frac{\partial \theta}{\partial \tau} = \frac{\partial^2 \theta}{\partial Z^2} \qquad \text{(Equation C-5)}$$

This equation is subject to the following boundary conditions, where K represents the partition coefficient:

$$\theta(Z,0) = 0 \qquad \text{(Equation C-6)}$$

$$\theta(0,\tau) = K \qquad \text{(Equation C-7)}$$

$$\dot{\theta}(1,\tau) = 0 \qquad \text{(Equation C-8)}$$

The solution, as calculated via finite Fourier transform is:

$$\theta(Z,\tau) = K - 2K\sum_{n=0}^{\infty} \frac{1}{\lambda_n}(e^{-\lambda_n^2 \tau})\sin(\lambda_n Z) \qquad \text{(Equation C-1)}$$

$$\lambda_n = \pi\left(n + \frac{1}{2}\right) \qquad \text{(Equation C-2)}$$

Data can be fit to the solution through a best fit for the partition coefficient and diffusion constant.

C.2 Magnetic Tweezers

It is also of interest to actively perturb the natural structure of biofilms. The ability to recover from a wide range of external disturbances makes biofilms hardy and difficult to treat, and it is important to understand if internal mechanical disruptions are also ineffective at permanently perturbing biofilms. We thus attempted to use magnetic

tweezers to perform active microrheology on biofilms to understand how an intact biofilm responds to internal perturbations. In particular, we were hoping to elicit a response of bacterial motion when beads were moved in the biofilm

C.2.1 Biofilm growth and incorporation of beads

Escherichia coli EMG2 and *E. coli* EMG2 with the plasmid pBBR1MCS5-eGFP were used to inoculate 3 mL of LB (lysogeny broth) or LB with 5 μg/mL gentamicin (Sigma) respectively and allowed to grow overnight. 100 μL of the static phase cultures was added to 3 mL of new growth medium and allowed to grow until the culture reached exponential phase (OD of ~0.8). The exponential phase cultures were combined in LB to a final OD_{600} of 0.05, in a 2:1 ratio of the EMG2 to the EMG2-GFP strain. This diluted culture was added to preformed wells constructed of PDMS bonded to a glass slide, with wells having a circular surface area, 4 mm in diameter. The cultures were grown at 37°C, without agitation, to allow for biofilm formation. At 40 hours of growth, 40 μL of a 0.1 v/v% dilution of stock 2.7 μm diameter, carboxylated magnetic beads (Invitrogen) was added onto the biofilm cultures. The beads were allowed to enter the biofilm for 1 hour.

C.2.2 Calibration of magnetic tweezers

Instead of using a traditional iron core/voltage source magnetic tweezer setup, we used cylindrical neodymium magnetics (Apex Magnets) to approach the sample. Magnetic tweezers are calibrated by moving magnetic beads through a fluid of known viscosity, with the tweezers and sample positioned as they would be during the actual experiment. In this case, we pulled 2.7 μm diameter, carboxylated magnetic beads (Invitrogen) through 55 v/v% glycerol in water, which has a viscosity of about 10 mPa*s at room temperature. To determine the force applied to a bead at a given location, the beads in the liquid are tracked, and the velocity is calculated, which allows for the determination of force by Stoke's Law:

$$F = 6\pi\mu vR \qquad \text{(Equation C-9)}$$

where F is the force applied by the magnet, μ is the dynamic viscosity, v is velocity, and R is the radius of the bead.

To track the beads, we used an Andor iXon3-885 EMCCD camera (Andor USA) with a 63x/1.4 NA oil immersion objective to produce bright field videos at a frame rate of 34.2 Hz with a shutter speed of 0.008 seconds. The trajectories were determined using publicly available Matlab codes (Kilfoil Group, http://people.umass.edu/kilfoil/downloads.html) with slight modification, and the velocity was calculated using code written in-house. This yielded a measured maximum force of $\sim 5*10^{-13}$ N for the above conditions.

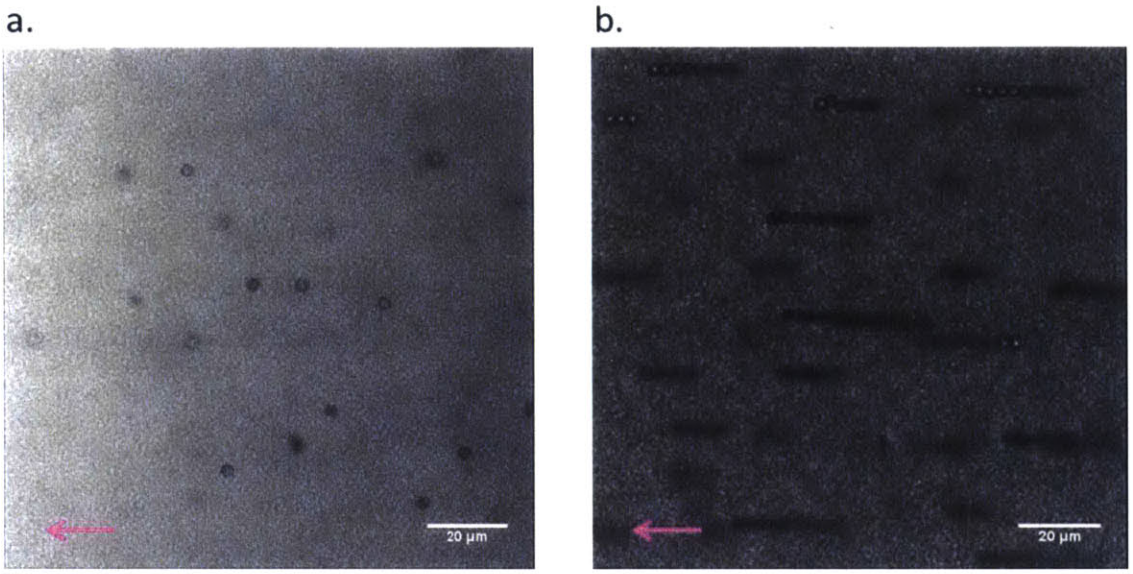

Figure C-2. Magnetic beads embedded in biofilms. (a) This image demonstrates individual beads that can be pulled through the biofilm in a localized manner. (b) Upon aggressive pulling of the beads with the magnet, they form chains of beads that move together through the biofilm. Arrows indicate the direction of pull. Scale bars are 20 microns.

C.2.3 Use of magnetic tweezers on biofilm

Moving the beads through the biofilm was achieved in the same manner as moving the beads through the glycerol solution. At first, an attempt was made to just move individual beads through the biofilm (Figure C-1a), but this yielded no significant perturbation to the system, and no bacterial motion. Thus, beads were moved in a more aggressive manner, leading to the formation of large chains of beads that moved through the biofilm (Figure C-1b). This again yielded little motion of the bacteria in the biofilm. However, in the videos, it seemed that as a snake of beads moved through the bacteria, the matrix closed up behind it in its wake. This is perhaps evidence of some of the self-healing behavior exhibited by biofilm, and could be explored further using the

magnetic tweezers. In addition, it may indicate that while the matrix is being perturbed by the beads, the bacteria are embedded strongly in it, so they do not release from the matrix just by being pushed around by the beads.

C.2.4 Other attempts at embedding magnetic beads

Multiple attempts were made at adding magnetic beads to biofilms grown under flow in capillary tubes. A flow system was made by mounting a 10 mL syringe onto a syringe pump, and attaching it via tubing to a square, glass capillary tube. The tube was connected to the capillary via epoxy. Tubing on the other end of the glass capillary went into a culture tube filled of bead/bacteria mixture in LB medium. Flow was set to 500 nl/min, to pull the medium through the tubing. Every 24 hours, the medium in the culture tube was changed out with fresh medium containing beads to ensure delivery of nutrients to the growing biofilm. However, when grown this way, the beads did not incorporate well into the biofilms, forming clumps near the bottom of the capillary. Clumps were seen with 2-μm diameter carboxylated magnetic beads in both *E. coli* and *Pseudomonas aeruginosa*. Similar results were achieved with 2-μm diameter aminated magnetic beads. Smaller, 1-μm diameter carboxylated beads also clumped in *E. coli* biofilm grown in this manner. Growing the bacteria under static conditions in the capillary did not improve incorporation of beads into the biofilms.

Bibliography

[1] Lieleg, O, Caldara, M, Baumgartel, R and Ribbeck, K 2011 *Soft Matter* **7** 3307-3314
[2] Darouiche, R O 2001 *Clinical Infectious Diseases* **33** 1567-1572
[3] Wilking, J N, Angelini, T E, Seminara, A, Brenner, M and Weitz, D A 2011 *MRS Bulletin* **36** 385-391
[4] Towler, B W, Rupp, C J, Cunningham, A B and Stoodley, P 2003 *Biofouling* **19** 279-285
[5] Pavlovsky, L, Younger, J G and Solomon, M J 2013 *Soft Matter* **9** 122-131
[6] Jones, W L, Sutton, M P, McKittrick, L and Stewart, P S 2011 *Biofouling* **27** 207-215
[7] Korstgens, V, Flemming, H C, Wingender, J and Borchard, W 2001 *Water Science and Technology* **43** 49-57
[8] Shaw, T, Winston, M, Rupp, C J, Klapper, I and Stoodley, P 2004 *Physical Review Letters* **93** e098102
[9] Korstgens, V, Flemming, H C, Wingender, J and Borchard, W 2001 *Journal of Microbiological Methods* **46** 9-17
[10] Houari, A, Picard, J, Habarou, H, Galas, L, Vaudry, H, Heim, V and Di Martino, P 2008 *Biofouling* **24** 235-240
[11] Stoodley, P, Lewandowski, Z, Boyle, J D and Lappin-Scott, H M 1999 *Biotechnology and Bioengineering* **65** 83-92
[12] Stoodley, P, Cargo, R, Rupp, C J, Wilson, S and Klapper, I 2002 *Journal of Industrial Microbiology & Biotechnology* **29** 361-367

[13] Klapper, I, Rupp, C J, Cargo, R, Purvedorj, B and Stoodley, P 2002 *Biotechnology and Bioengineering* **80** 289-296
[14] Dunsmore, B C, Jacobsen, A, Hall-Stoodley, L, Bass, C J, Lappin-Scott, H M and Stoodley, P 2002 *Journal of Industrial Microbiology & Biotechnology* **29** 347-353
[15] Cense, A W, Peeters, E A G, Gottenbos, B, Baaijens, F P T, Nuijs, A M and van Dongen, M E H 2006 *Journal of Microbiological Methods* **67** 463-472
[16] Poppele, E H and Hozalski, R M 2003 *Journal of Microbiological Methods* **55** 607-615
[17] Aggarwal, S, Poppele, E H and Hozalski, R M 2010 *Biotechnology and Bioengineering* **105** 924-934
[18] Aggarwal, S and Hozalski, R M 2010 *Biofouling* **26** 479-486
[19] Flemming, H C and Wingender, J 2010 *Nature Reviews Microbiology* **8** 623-633
[20] Branda, S S, Vik, Å, Friedman, L and Kolter, R 2005 *Trends in Microbiology* **13** 20-26
[21] Wozniak, D J, Wyckoff, T J O, Starkey, M, Keyser, R, Azadi, P, O'Toole, G A and Parsek, M R 2003 *Proceedings of the National Academy of Sciences of the United States of America* **100** 7907-7912
[22] Matsukawa, M and Greenberg, E P 2004 *Journal of Bacteriology* **186** 4449-4456
[23] Friedman, L and Kolter, R 2004 *Journal of Bacteriology* **186** 4457-4465
[24] Colvin, K M, Irie, Y, Tart, C S, Urbano, R, Whitney, J C, Ryder, C, Howell, P L, Wozniak, D J and Parsek, M R 2012 *Environmental Microbiology* **14** 1913-1928
[25] Karatan, E and Watnick, P 2009 *Microbiology and Molecular Biology Reviews* **73** 310-347
[26] Wimpenny, J W T and Colasanti, R 1997 *FEMS Microbiology Ecology* **22** 1-16
[27] Hall-Stoodley, L, Costerton, J W and Stoodley, P 2004 *Nature Reviews Microbiology* **2** 95-108
[28] Chen, M J, Zhang, Z and Bott, T R 1998 *Biotechnology Techniques* **12** 875-880
[29] Chen, M J, Zhang, Z and Bott, T R 2005 *Colloids and Surfaces B: Biointerfaces* **43** 61-71
[30] Lau, P C Y, Dutcher, J R, Beveridge, T J and Lam, J S 2009 *Biophysical Journal* **96** 2935-2948
[31] Macnab, R M 2003 *Annual Review of Microbiology* **57** 77-100
[32] Stocker, R, Seymour, J R, Samadani, A, Hunt, D E and Polz, M F 2008 *Proceedings of the National Academy of Sciences of the United States of America* **105** 4209-4214
[33] Dennis, P G, Seymour, J, Kumbun, K and Tyson, G W 2013 *The ISME journal* **7** 1661-1664
[34] Morrison, F A 2001 *Understanding Rheology*. Oxford University Press, New York.
[35] Squires, T M and Mason, T G 2010 *Annual Review of Fluid Mechanics* **42** 413-438
[36] Macosko, C W 1994 *Rheology: Principles, Measurements, and Applications*. VCH Publishers, Inc., New York.
[37] Ohashi, A and Harada, H 1994 *Water Science and Technology* **29** 281-288
[38] Barnes, H A, Hutton, J F and Walters, K 1989 *An Introduction to Rheology*. Elsevier Science Publishers B.V., Amsterdam.
[39] Bird, R B, Armstrong, R C and Hassager, O 1987 *Dynamics of Polymeric Liquids: Volume 1 Fluid Mechanics*. John Wiley and Sons, New York.
[40] Rubinstein, M and Colby, R H 2003 *Polymer Physics*. Oxford University Press, Oxford.
[41] Ewoldt, R H, Winter, P, Maxey, J and McKinley, G H 2010 *Rheologica Acta* **49** 191-212

[42] Hyun, K, Kim, S H, Ahn, K H and Lee, S J 2002 *Journal of Non-Newtonian Fluid Mechanics* **107** 51-65
[43] Barnes, H A 1999 *Journal of Non-Newtonian Fluid Mechanics* **81** 133-178
[44] Nguyen, Q D and Boger, D V 1992 *Annual Review of Fluid Mechanics* **24** 47-88
[45] Hohne, D N, Younger, J G and Solomon, M J 2009 *Langmuir* **25** 7743-7751
[46] Mason, T G and Weitz, D A 1995 *Physical Review Letters* **74** 1250-1253
[47] MacKintosh, F C and Schmidt, C F 1999 *Current Opinion in Colloid & Interface Science* **4** 300-307
[48] Crocker, J C and Grier, D G 1996 *Journal of Colloid and Interface Science* **179** 298-310
[49] Savin, T and Doyle, P S 2005 *Biophysical Journal* **88** 623-638
[50] Mason, T G, Ganesan, K, van Zanten, J H, Wirtz, D and Kuo, S C 1997 *Physical Review Letters* **79** 3282-3285
[51] Mason, T G 2000 *Rheologica Acta* **39** 371-378
[52] Zhu, X Y, Kundukad, B and van der Maarel, J R C 2008 *Journal of Chemical Physics* **129**
[53] Wirtz, D 2009 *Annual Review of Biophysics* **38** 301-326
[54] Rogers, S S, van der Walle, C and Waigh, T A 2008 *Langmuir* **24** 13549-13555
[55] Galy, O, Latour-Lambert, P, Zrelli, K, Ghigo, J M, Beloin, C and Henry, N 2012 *Biophysical Journal* **103** 1400-1408
[56] Conrad, J C, Gibiansky, M L, Jin, F, Gordon, V D, Motto, D A, Mathewson, M A, Stopka, W G, Zelasko, D C, Shrout, J D and Wong, G C 2011 *Biophysical Journal* **100** 1608-1616
[57] Qian, C, Wong, C C, Swarup, S and Chiam, K H 2013 *Applied and Environmental Microbiology* **79** 4734-4743
[58] Cheong, F C, Duarte, S, Lee, S H and Grier, D G 2009 *Rheologica Acta* **48** 109-115
[59] Forier, K, Messiaen, A S, Raemdonck, K, Deschout, H, Rejman, J, De Baets, F, Nelis, H, De Smedt, S C, Demeester, J, Coenye, T *et al.* 2012 *Nanomedicine (Lond)* **8** 939-945
[60] De Beer, D, Stoodley, P and Lewandowski, Z 1994 *Biotechnology and Bioengineering* **44** 636-641
[61] Stoodley, P, Yang, S N, LappinScott, H and Lewandowski, Z 1997 *Biotechnology and Bioengineering* **56** 681-688
[62] Messiaen, A-S, Forier, K, Nelis, H, Braeckmans, K and Coenye, T 2013 *PLoS ONE* **8** e79220
[63] Waigh, T A 2005 *Reports on Progress in Physics* **68** 685-742
[64] Rich, J P, Lammerding, J, McKinley, G H and Doyle, P S 2011 *Soft Matter* **7** 9933-9943
[65] Zrelli, K, Galy, O, Latour-Lambert, P, Kirwan, L, Ghigo, J M, Beloin, C and Henry, N 2013 *New Journal of Physics* **15** 125026
[66] Binnig, G, Quate, C F and Gerber, C 1986 *Physical Review Letters* **56** 930-933
[67] Ahimou, F, Semmens, M J, Novak, P J and Haugstad, G 2007 *Applied and Environmental Microbiology* **73** 2897-2904
[68] Billings, N, Birjiniuk, A, Samad, T S, Doyle, P S and Ribbeck, K 2015 *Reports on Progress in Physics* **78** 036601
[69] Birjiniuk, A, Billings, N, Nance, E, Hanes, J, Ribbeck, K and Doyle, P S 2014 *New Journal of Physics* **16** 085014
[70] Fernandez, A S, Hashsham, S A, Dollhopf, S L, Raskin, L, Glagoleva, O, Dazzo, F B, Hickey, R F, Criddle, C S and Tiedje, J M 2000 *Applied and Environmental Microbiology* **66** 4058-4067

[71] Hosni, T, Moretti, C, Devescovi, G, Suarez-Moreno, Z R, Fatmi, M B, Guarnaccia, C, Pongor, S, Onofri, A, Buonaurio, R and Venturi, V 2011 *The ISME Journal* **5** 1857-1870
[72] Burmolle, M, Ren, D W, Bjarnsholt, T and Sorensen, S J 2014 *Trends in Microbiology* **22** 84-91
[73] McFall-Ngai, M, Hadfield, M G, Bosch, T C G, Carey, H V, Domazet-Loso, T, Douglas, A E, Dubilier, N, Eberl, G, Fukami, T, Gilbert, S F *et al.* 2013 *Proceedings of the National Academy of Sciences of the United States of America* **110** 3229-3236
[74] Turnbaugh, P J, Ley, R E, Hamady, M, Fraser-Liggett, C M, Knight, R and Gordon, J I 2007 *Nature* **449** 804-810
[75] Chambers, H F 2001 *Emerging Infectious Diseases* **7** 178-182
[76] Bauer, T M, Ofner, E, Just, H M, Just, H and Daschner, F D 1990 *The Journal of Hospital Infection* **15** 301-309
[77] Hunter, P, Dalby, J, Marks, J, Swain, G R and Schrager, S 2014 *Primary Care* **41** 215-237
[78] Virji, M 2009 *Nature Reviews Microbiology* **7** 274-286
[79] Musher, D M 2003 *The New England Journal of Medicine* **348** 1256-1266
[80] Gralton, J, Tovey, E, McLaws, M L and Rawlinson, W D 2011 *The Journal of Infection* **62** 1-13
[81] Adler, J 1976 *Journal of Supramolecular Structure* **4** 305-317
[82] Berg, H C 1975 *Annual Review of Biophysics and Bioengineering* **4** 119-136
[83] Ottemann, K M and Miller, J F 1997 *Molecular Microbiology* **24** 1109-1117
[84] Josenhans, C and Suerbaum, S 2002 *International Journal of Medical Microbiology* **291** 605-614
[85] Bucior, I, Pielage, J F and Engel, J N 2012 *PLoS Pathogens* **8** e1002616
[86] Roy, K, Hilliard, G M, Hamilton, D J, Luo, J, Ostmann, M M and Fleckenstein, J M 2009 *Nature* **457** 594-598
[87] O'Toole, P W, Lane, M C and Porwollik, S 2000 *Microbes and Infection / Institut Pasteur* **2** 1207-1214
[88] Freney, J, Kloos, W E, Hajek, V, Webster, J A, Bes, M, Brun, Y and Vernozy-Rozand, C 1999 *International Journal of Systematic Bacteriology* **49 Pt 2** 489-502
[89] Kloos, W E and Bannerman, T L 1994 *Clinical Microbiology Reviews* **7** 117-140
[90] Cole, A M, Tahk, S, Oren, A, Yoshioka, D, Kim, Y H, Park, A and Ganz, T 2001 *Clinical and Diagnostic Laboratory Immunology* **8** 1064-1069
[91] Otto, M 2010 *Expert Review of Dermatology* **5** 183-195
[92] Peacock, S J, de Silva, I and Lowy, F D 2001 *Trends in Microbiology* **9** 605-610
[93] Lindberg, E, Adlerberth, I, Hesselmar, B, Saalman, R, Strannegard, I L, Aberg, N and Wold, A E 2004 *Journal of Clinical Microbiology* **42** 530-534
[94] Matthäus, F, Jagodič, M and Dobnikar, J 2009 *Biophysical Journal* **97** 946-957
[95] Malone, C L, Boles, B R, Lauderdale, K J, Thoendel, M, Kavanaugh, J S and Horswill, A R 2009 *Journal of Microbiological Methods* **77** 251-260
[96] Elbing, K and Brent, R 2002, *Current Protocols in Molecular Biology*. John Wiley & Sons, Inc., Vol. 59, pp. 1.1.1-1.1.7.
[97] Merritt, J H, Kadouri, D E and O'Toole, G A 2011, *Current Protocols in Microbiology*. John Wiley & Sons, Inc, pp. 1B.1.1-1B.1.18.
[98] Savin, T, Spicer, P T and Doyle, P S 2008 *Applied Physics Letters* **93**
[99] Ha, D-G, Kuchma, S and O'Toole, G 2014 In Filloux, A. and Ramos, J.-L. (eds.), *Pseudomonas Methods and Protocols*. Springer New York, Vol. 1149, pp. 67-72.
[100] Kaito, C and Sekimizu, K 2007 *Journal of Bacteriology* **189** 2553-2557
[101] Lauga, E and Powers, T R 2009 *Reports on Progress in Physics* **72**

[102] Lauffenburger, D A 1991 *Microbial Ecology* **22** 175-185
[103] Wong, C C, Qian, C and Chiam, K H 2013 *Biophysical Journal* **104** 639A-640A
[104] Sibley, C D, Parkins, M D, Rabin, H R, Duan, K, Norgaard, J C and Surette, M G 2008 *Proceedings of the National Academy of Sciences of the United States of America* **105** 15070-15075
[105] Huttenhower, C, Gevers, D, Knight, R, Abubucker, S, Badger, J H, Chinwalla, A T, Creasy, H H, Earl, A M, FitzGerald, M G, Fulton, R S *et al.* 2012 *Nature* **486** 207-214
[106] Strom, S L 2008 *Science* **320** 1043-1045
[107] Grossart, H P, Dziallas, C, Leunert, F and Tang, K W 2010 *Proceedings of the National Academy of Sciences of the United States of America* **107** 11959-11964
[108] Ingham, C J, Kalisman, O, Finkelshtein, A and Ben-Jacob, E 2011 *Proceedings of the National Academy of Sciences of the United States of America* **108** 19731-19736
[109] Ma, L, Conover, M, Lu, H, Parsek, M R, Bayles, K and Wozniak, D J 2009 *PLoS Pathog*ens**5** e1000354
[110] Ryder, C, Byrd, M and Wozniak, D J 2007 *Current Opinion in Microbiology* **10** 644-648
[111] Friedman, L and Kolter, R 2004 *Molecular Microbiology* **51** 675-690
[112] Kaplan, J B 2010 *Journal of Dental Research* **89** 205-218
[113] Davies, D G and Marques, C N H 2009 *Journal of Bacteriology* **191** 1393-1403